Examining Melt Pond Dynamics and Light Availability in the Arctic Ocean via High Resolution Satellite Imagery

Austin Wesley Abbott
Old Dominion University, abbot189@umn.edu

EXAMINING MELT POND DYNAMICS AND LIGHT AVAILABILITY IN

THE ARCTIC OCEAN VIA HIGH RESOLUTION SATELLITE

IMAGERY

by

Austin Wesley Abbott
B.S. August 2017, University of Minnesota

A Thesis Submitted to the Faculty of
Old Dominion University in Partial Fulfillment of the
Requirements for the Degree of

MASTER OF SCIENCE

OCEAN AND EARTH SCIENCES

OLD DOMINION UNIVERSITY
August 2021

Approved by:

Victoria J. Hill (Director)

Richard C. Zimmerman (Member)

Sophie Clayton (Member)

ABSTRACT

EXAMINING MELT POND DYNAMICS AND LIGHT AVAILABILITY IN THE ARCTIC OCEAN VIA HIGH RESOLUTION SATELLITE IMAGERY

Austin Wesley Abbott
Old Dominion University, 2021
Director: Dr. Victoria J. Hill

As the Arctic experiences consequences of climate change, a shift from thicker, multi-year ice to thinner, first-year ice has been observed. First-year ice is prone to extensive pools of meltwater ("melt ponds") forming on its surface, which enhance light transmission to the ocean. Changes in the timing and distribution of melt pond formation and associated increases in under-ice light availability are the primary drivers for seasonal progression of water column primary production and warming. Observations of melt pond development and distribution require meter scale resolution and have traditionally been limited to airborne images. However, recent advances in high spatial resolution satellites now allow for observations of individual melt ponds from space.

Images of pack ice in the Chukchi Sea during 2018 obtained from WorldView satellite systems showed minimal melt pond coverage in June, with a rapid increase in late June, leading to saturated and flooded ice floes by mid-July. Cumulative hours above freezing (air temperature) was a stronger predictor for pond development than daily average values of temperature and irradiance and was well represented by a logistic growth curve.

Size distributions (normalized to total pond area) of melt pond area was dominated by small (≤ 10 m^2) ponds at the onset of ponding, shifting towards medium sized ponds (mode of 100 to 1,000 m^2) as surface melt progressed. Late in the summer when ice flows were saturated

with ponds, the distribution was skewed towards a handful of very large ponds nearing 1,000,000 m^2, connected by channels which created a myriad of complex shapes.

A primary production model driven by under-ice light intensity estimated from our classified images revealed that initial small increases in melt pond fraction have a large impact on potential under-ice chlorophyll growth and carbon uptake, eventually trending towards a saturating upper limit as ponds continued to spread. Results shown here offer novel insights into melt pond growth and distribution, along with estimates of how ponding impacts primary production. These conclusions showcase physical, observable consequences of an Arctic Ocean dominated by thin, first-year ice, and can be employed to advise future efforts in Arctic modeling.

This thesis is dedicated to my late grandfather, Warren "Bud" Abbott. His examples of steadfast

love and faith inspire me to be a better man.

ACKNOWLEDGEMENTS

There are so many people that have supported me through this process and during my time as a graduate student. To my advisor, Dr. Victoria Hill, thank you for responding to my cold call email 4 years ago and taking a chance on me as a student. Thank you for your continued support and guidance through the research and writing process. To my committee members, Dr. Richard C. Zimmerman and Dr. Sophie Clayton, thank you for your amazing instruction on various disciplines that will serve me well in my future career. To Brian Collister and the rest of the BORG lab crew, thank you for your feedback and support throughout this process.

To my amazing wife Kaitlyn, my Mom, Dad, and sister Shealyn, thank you for your unending love and support through not only my thesis, but also in helping me navigate so many personal challenges over the last few years. To my best boy Tango, thank you for the tail wags, cuddles, and hiking adventures. To all my friends in the Norfolk area and back home in Minnesota, thank you for all the dinners, drinks, cigars, zoom calls, and other fun times that provided much needed distractions from studying melt ponds.

NOMENCLATURE

AT	Air Temperature, $^{\circ}$C
DMP	Dark Melt Pond
$E_d(0^-)$	Downwelling Irradiance just below the Ice/Water or Air/Water Interface, mol m^{-2} d^{-1}
EVWHS	Enhanced View Web Hosting Services
f_{pi}	Pond Fraction of Ice
f_{ps}	Pond Fraction of Scene
FYI	First-Year Ice
LMP	Light Melt Pond
MIZ	Marginal Ice Zone
MLC	Maximum Likelihood Classification
MYI	Multi-Year Ice
NSIDC	National Snow and Ice Data Center
PAR	Photosynthetically Available Radiation
RGB	Red-Green-Blue
ROI	Region of Interest
SK	Sidekick
SST	Sea Surface Temperature, $^{\circ}$C
WARM	Warming and Irradiance Measurements
WB	WARM Buoy
WV	WorldView (satellites)

TABLE OF CONTENTS

LIST OF TABLES

LIST OF FIGURES

INTRODUCTION

Changes in the Arctic Environment

The Arctic Ocean is a region with a rapidly changing climate, resulting in sea ice decrease over decadal timescales. Thicker, multi-year ice (MYI) has been replaced by thinner, seasonal first year ice (FYI) at an alarming rate, with decreases in MYI ranging from 15.1% to 17.2% per decade (Comiso, 2011). The Arctic is experiencing earlier ice melt and break-up in the spring, and delayed re-freeze in the fall when compared to historical data (Johnson & Eicken, 2016; Richter-Menge & Druckenmiller, 2020).

The transition to FYI results in lower surface albedo, reduced snow cover, enhanced melting, and greater input of solar radiation both into the ice and reaching the upper water column (Perovich & Polashenski, 2012). Submarine light availability in ice covered waters is largely attenuated by the high scattering nature of the overlying ice pack, which contains air bubbles and brine channels with different refractive indices than the surrounding ice (Mobley et al., 1998). Additionally, the age of the sea ice has a large impact on its transmissivity. FYI can boost light transmission to the water column nearly three-fold in comparison to MYI, from 4% to 11% (Nicolaus et al., 2012), creating a more conducive environment for light driven processes. In 2011 the Arctic was comprised of 44% MYI and 56% FYI. Replacement of all remaining MYI with FYI is predicted to increase mean transmitted energy flux by 18% (Arndt & Nicolaus 2014).

Phytoplankton blooms have been observed underneath thin and ponded ice as early as June, suggesting that these conditions provide ample light to support photosynthesis before the ice completely melts in late July to early August (Arrigo et al., 2014; Assmy et al., 2017; Hill et

al., 2018). A shift from historic open water phytoplankton blooms in July and August to earlier under ice blooms in May and June has the potential to cause a phenological mismatch, where phytoplankton blooms occur before zooplankton have reached the feeding stage, leading to starvation and low recruitment rates (Ji et al., 2013). Alternatively, increased grazing may limit export production to the benthos, resulting in the decline of bivalves and other benthic organisms that serve as key food sources for larger organisms (Grebmeier, 2012).

Melt Ponds

As snow and ice begin to melt in the late spring and early summer, surface ponding of the meltwater (hereafter referred to as "melt ponds") begins to occur in areas of low local topography (Polashenski et al., 2012). Melt ponds can become widespread at lower latitudes (70° – 80° N) but have been observed as far as 88° N (Huang et al., 2016). There is some variability in the development and propagation of melt ponds. MYI seems to undergo less ponding than FYI (Nicolaus et al., 2012), which typically becomes saturated with a complex network of interconnected ponds by late summer (Fetterer & Untersteiner, 1998; Tschudi et al., 2001; Webster et al., 2015). Ponds on MYI tend to be of a lighter color (Buckley et al., 2020), which is most likely attributable to the underlying ice type (Tschudi et al., 2001). The degree to which ponding occurs is partially a function of the roughness and thickness of local sea ice (Nasonova et al., 2018). There is general agreement that ponding is a dynamic process controlled by multiple drivers and should be expected to vary geographically and interannually (Eicken et al., 2002; Perovich et al., 2002b; Perovich & Polashenski, 2012; Tschudi et al., 2008).

Pond development has conventionally been addressed in four separate stages (Eicken et al., 2002). Initially, air temperatures above 0° C drive snow and ice melt, which causes

widespread lateral ponding (Stage I). As the summer progresses, increased ice permeability

allows melt pond drainage through the ice, thus lowering pond fraction (Stage II). Stage III is

marked by reduced freeboard (difference in height between sea surface and ice surface) and

extensive ponding on the ice, with ponds that melt all the way through to the underlying water

column. Stage IV marks freeze-up and is accompanied by a steep decrease in pond fraction.

Similar stages were later re-defined by Perovich & Polashenski (2012).

Consequences of Melt Ponds

Melt pond formation and decreased snow cover both lower the albedo of the ice pack,

resulting in warming and thermal expansion of seawater (Perovich et al., 2008). Longer periods

of reduced ice cover can drive up temperature in the upper water column, thus increasing

stratification (Perovich & Maykut, 1990), which can limit nutrient availability. Greater UV

penetration also leads to increased photochemical oxidation of dissolved organic matter. This

can result in a release of CO_2 to the atmosphere (Sulzberger & Arey, 2016) and increase the

abundance of biologically available products (Kieber et al, 1989).

Arguably the greatest consequence of melt pond formation is the increased amount of

light reaching the upper water column (Frey et al., 2011; Light et al., 2008; Light et al., 2015;

Perovich et al., 1998a). Ice type, pond fraction, and melt onset are the main drivers affecting

light availability beneath the ice (Arndt & Nicolaus, 2014). When the Arctic seasonal ice pack

begins to melt and retreat, extreme heterogeneity is seen in light penetration to the ocean due to

variations in surface snow melt, and the distribution of ponded ice and open water leads (Frey et

al., 2011). It is therefore very challenging to estimate the time-integrated light dose that

phytoplankton may experience as they drift under the ice. Estimates of productivity can easily

become complex, as the continuous movement of both water and ice allows the upper water column to experience large and rapid temporal variations in the quantity and quality of light. These estimates are further complicated by the difficulty of obtaining large scale in situ measurements of pond presence and size. New methods with the capability of covering large areas at meter scale spatial resolution will be required to advance the monitoring of melt pond development.

Measuring Melt Pond Abundance

Aerial imagery has long been the preferred method for observing and quantifying melt pond coverage. The difference in spectral reflectance characteristics between bright ice, dark water, and intermediate melt ponds allows for the separation of melt ponds from surrounding ice pixels. High resolution cameras mounted on aircraft can provide 2-D images of the ice surface for feature classification but are limited to collecting data along transects spanning the swath width of the camera at flight altitude (Buckley et al., 2020; Derksen et al., 1997; Eicken et al., 2002; Huang et al., 2016; Perovich & Tucker, 1997; Perovich et al., 2002b; Tschudi et al., 2001; Yackel et al., 2000 and others). Additionally, continuous aerial surveys require a large investment of resources and labor to obtain seasonal time series of melt pond development.

Observations of individual melt ponds requires imagery with spatial resolution on the scale of meters or better. This disqualifies many spaceborne remote sensing systems, such as VIIRS (Visible Infrared Imaging Radiometer Suite) with a spatial resolution of 750 m, and passive microwave measurements used to quantify ice concentration by the NSIDC (National Snow and Ice Data Center) (25-kilometer footprint). Accurate estimations of pond fraction have been carried out with MODIS (MODerate resolution Imaging Spectroradiometer) via area-

averaged reflectance values validated by UAV imagery (Tschudi et al., 2008). However, with a spatial resolution of 250 m, MODIS still lacks the ability to quantify the size, shape, depth and spatial extent of individual ponds.

A handful of previous studies have successfully classified melt ponds using satellite imagery with higher spatial resolution. Fetterer & Untersteiner (1998) and Webster et al. (2015) both used National Technical Means (NTM) satellite imagery (single panchromatic band, 1 m resolution) to obtain melt pond aerial coverage. Nasonova et al. (2018) utilized the GeoEye-1 satellite (2 m multiband resolution, 0.5 m panchromatic resolution) operated by MAXAR© to calculate pond fraction. Of these, Fetterer & Untersteiner (1998) and Nasonova et al. (2018) successfully employed maximum likelihood classifications- supervised classification techniques that use manually selected training areas to map melt pond distribution. Webster et al. (2015) designed a custom classification based on object histograms.

Though computer-based image classifications can be powerful tools for quantification of melt ponds, they are subject to error. Buckley et al. (2020) observed five common features that cause misclassifications- ridge shadows, sun glint from waves, ice draft (submerged ice edge), open water near melt ponds, and very light melt ponds. Perovich et al. (2002b) also noted that bottomless melt ponds can be classified as open water due to their dark color. Derksen et al. (1997) recorded difficulty in distinguishing between shallow melt ponds and wet snow. While often observed, all these errors were concluded to have minimal effects on classification results. Snow ridges and waves amidst large open water patches occurred so infrequently that even 100% misclassification would have minor impacts on overall interpretation of the images (Buckley et al., 2020).

Motivation for this Study

Changes in the Arctic seasonal landscape have driven numerous melt pond studies over the past 25 years. The melting dynamics of a system primarily dominated by drifting FYI are poorly constrained and should not be assumed to follow the same patterns observed on MYI or landfast ice (connected to the terrestrial environment) (Webster et al., 2015). Large scale observations of an entire region that span a complete seasonal melt cycle also remain sparse. Fetterer & Untersteiner (1998) postulated that study sites should be greater than 30 km^2 to truly minimize landscape variability. This conclusion demands remote sensing imagery taken at high altitude, capable of observing systems that are tens or hundreds of square kilometers in size. The inherent ease of quantifying melt pond abundance from space also offers a more cost and time effective alternative to the investigator, as opposed to months of repeated flights over the ice.

The Chukchi Sea is a highly studied region given its shallow shelf, high nutrient load, and high primary production (Arrigo et al., 2017). Additionally, the Chukchi Sea is undergoing drastic changes in ice cover and experiencing anomalously high sea surface temperatures (SST) (Richter-Menge & Druckenmiller, 2020). Increased light availability earlier in the year has the possibility to prematurely kickstart phytoplankton blooms, potentially altering the biogeochemistry of the region. The large-scale study of melt ponds is an evolving research field, and thus the construction of additional melt pond time-series can provide much needed insight into the melt cycle of data poor regions. Therefore, the following goals were identified for further investigation.

1) *Determine the ability of high-resolution multiband satellite imagery to identify and classify melt ponds.*

2) *Use satellite imagery to quantify seasonal melt pond abundance, spatial characteristics, and determine the main environmental drivers of melt pond development.*

3) *Predict light availability under various degrees of ponded ice to aid in improving Arctic primary production modeling efforts.*

4) *Quantify the advantages of using commercial high-resolution images relative to coarser, publicly available data sets to explore how spatial resolution impacts endmember data.*

METHODS

WorldView Satellites & Image Collection

WorldView 2 and WorldView 3 (WV-2 & WV-3) are high spatial resolution satellites owned and operated by Digital Globe (MAXAR©), which can provide pan-sharpened RGB (Red-Green-Blue) or 8-band (non-atmospherically corrected) imagery with sub-meter scale spatial resolution (0.46 & 0.31 meters, respectively). These systems are capable of discerning individual melt ponds and observing their associated spectral reflectance characteristics, thus allowing for estimates of pond size and distribution patterns.

Satellite images of sea ice in the Chukchi Sea from spring and summer 2018 were collected by WV-2 & WV-3. These satellites were specifically tasked to collect images in the proximity of two autonomous buoys (referred to as WARM Buoy 7 & 8) that were deployed in the northern Chukchi Sea in March of 2018 as part of an NSF funded project (Hill et al., 2019) (Figure 1). Tasking was handled by NASA and the Polar Geospatial Center at the University of Minnesota, who had access to the buoy locations, and was supported by NSF Grant No. 1603548. Due to varying speed of the drifting ice pack, the collections were not always co-incident with the exact buoy locations (Table 1).

Image data were accessed through Enhanced View Web Hosting Services (EVWHS) (https://evwhs.digitalglobe.com/). A shape file encompassing much of the Chukchi Sea was uploaded to the EVWHS search bar to locate and select relevant scenes. All images in this study were obtained as radiometrically calibrated GeoTIFF files. Amazon Web Services' (AWS) S3 console was used to facilitate file transfer. All images, documentation, and supporting files were pushed directly from the EVWHS imagery cart to the S3 console, and then downloaded in a zipped folder from AWS.
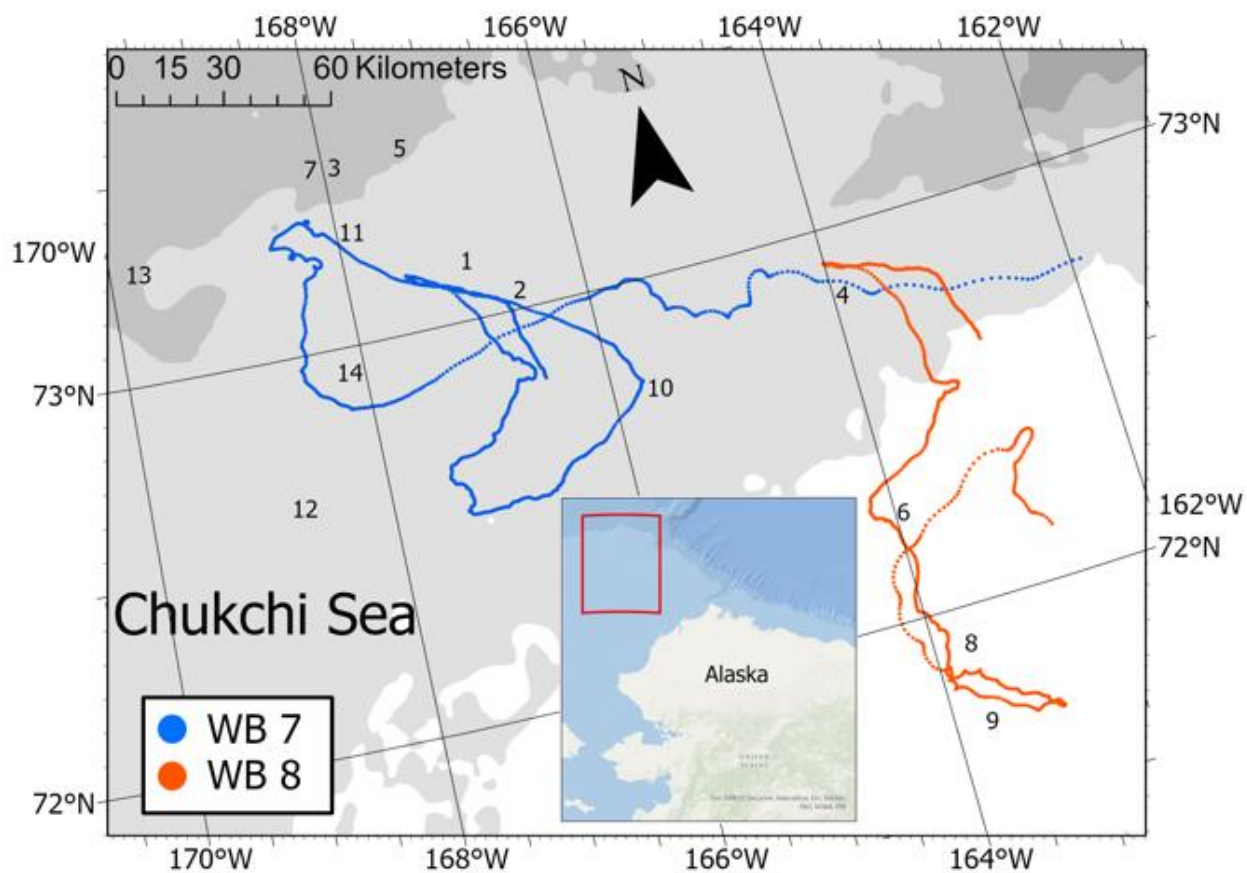
Figure 1: Study Site. Map showing the paths of WARM Buoy 7 (WB7) and WARM Buoy 8 (WB8) throughout the time-period of usable WV imagery (June 1st – July 20th), with WV image locations represented as numbers that correspond to Table 1.

Images from March through August 2018 were available for download from EVWHS. After visual inspection, full analysis was limited to the period when melt ponds were present - June 1st to July 20th, from which there were 14 scenes collected on 10 individual days (Table 1). Images (scenes) were broken into multiple tiles by EVWHS when downloaded due to the large file sizes associated with high resolution data (Figure 2). Image tiles on the edge of a scene were surrounded by black pixels with zero values for all 3 bands. This is a result of forcing an angled

parallelogram scene to fill a rectangular space. These pixels were masked by adding a "Data Ignore Value" of zero into the metadata.

Table 1*:* **Catalog of Available Satellite Images.** Available WV imagery used for this project. Corresponding buoy refers to the in-situ WARM buoy that was closest to a WV scene. Distance was calculated between the average position of the buoy on a given calendar day, and the center of the associated WV scene. Note that most WV images are tens of kilometers across.

Image Number	Image Date	Corresponding Buoy (7 or 8)	Distance to Closest Buoy (km)	Scene Area (km^2)	Sensor
1	6/1/2018	7	37	582	WV-2
2	6/4/2018	7	55	1,253	WV-2
3	6/4/2018	7	10	1,059	WV-2
4	6/5/2018	8	11	1,010	WV-2
5	6/5/2018	7	47	492	WV-3
6	6/18/2018	8	3	299*	WV-2
7	6/22/2018	7	82	1,023	WV-3
8	6/22/2018	8	13	707	WV-3
9	6/26/2018	8	19	828	WV-2
10	6/27/2018	7	9	700	WV-2
11	6/28/2018	7	79	1,179	WV-2
12	7/13/2018	7	71	154	WV-3
13	7/13/2018	7	101	492	WV-3
14	7/20/2018	7	185	48*	WV-2

*Partial scene used due to cloudiness in image.
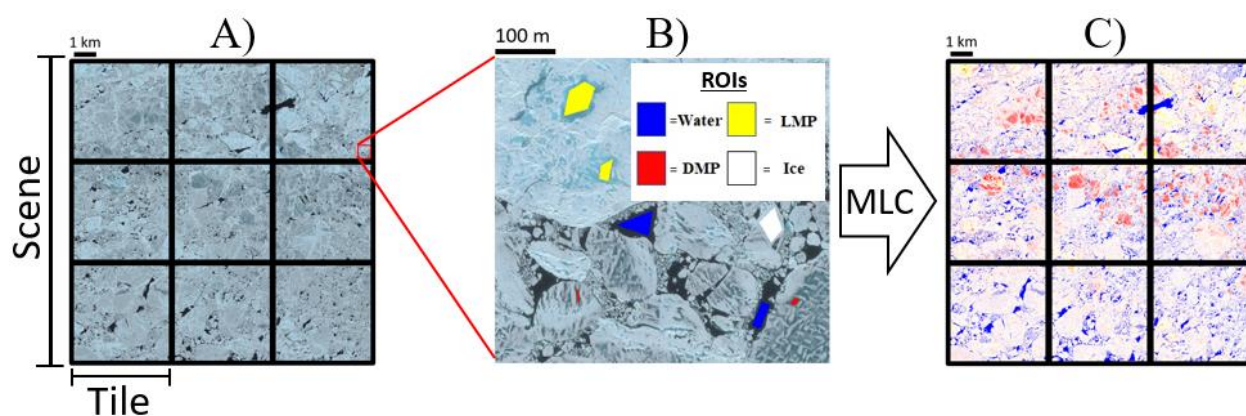
Figure 2: Workflow Schematic. A. Each scene is comprised of multiple tiles. B. ROI's (regions of interest) are defined from within one tile from each scene. C. These ROIs were then used to train the computer to classify the entire scene using a Maximum Likelihood Classifier (MLC).

Supervised Image Classification

Visual inspection of the images showed four distinct classes: ice, open water, light melt pond (LMP), and dark melt pond (DMP). Spectral differences in LMP and DMP were most likely driven by underlying ice type (Buckley et al., 2020; Tschudi et al., 2001; Webster et al., 2015). Such separation of the melt pond class into light and dark ponds is a common practice (Buckley et al., 2020; Yackel et al., 2000). The differences in class spectra suggest that classification can be successfully carried out with pan-sharpened RGB imagery, as there is little to no overlap between any two classes across all three bands (Figure 3). WV also offers an uncorrected 8-band product, which was not included in this study. Attempts were made to

perform an atmospheric correction on the 8-band imagery via the dark pixel subtraction method (Chavez, 1996) but proved to be unsuccessful. Large, bright flows of ice consistently contaminated the signal from adjacent "dark water" pixels.

A minimum of three training patches (Regions of Interest or "ROIs") per class per scene were defined with the ENVI software package (version 5.5), and then used to train the classifier with a supervised classification model. Redefining ROIs for each scene was necessary as no atmospheric correction was applied to the images, resulting in varying class band values between images. Including an adequate number of pixels in the training blocks is important for obtaining good classification results (Chen and Stow, 2002). The median number of training pixels per class per scene in this study was 6,621. However, in cases where all the ROIs in a class are spectrally homogenous, good classifications can be achieved with far smaller training areas. Though some variability in training patch sizes did exist between classes here (a patch of ice or open water is usually larger than a melt pond), there were consistently enough training pixels to constrain each of the classes such that their range of values across the spectrum were distinct from one another (Figure 3).

The Maximum Likelihood Classification module (MLC) was applied to all images. The maximum likelihood method is widely employed for classifying multispectral imagery and uses the means and variances from training data to calculate the probability that each pixel belongs to a given class (Perumal and Bhaskaran, 2010). Previous studies have successfully employed MLCs for pond identification (Fetterer & Untersteiner, 1998; Nasonova et al., 2018). One tile from each scene was used to collect ROIs (Figure 2A & 2B). These training patches were then used to classify all tiles within the scene (Figure 2C). As no atmospheric correction was applied

to the images, only tiles within the same scene were spectrally consistent. Thus, a new set of

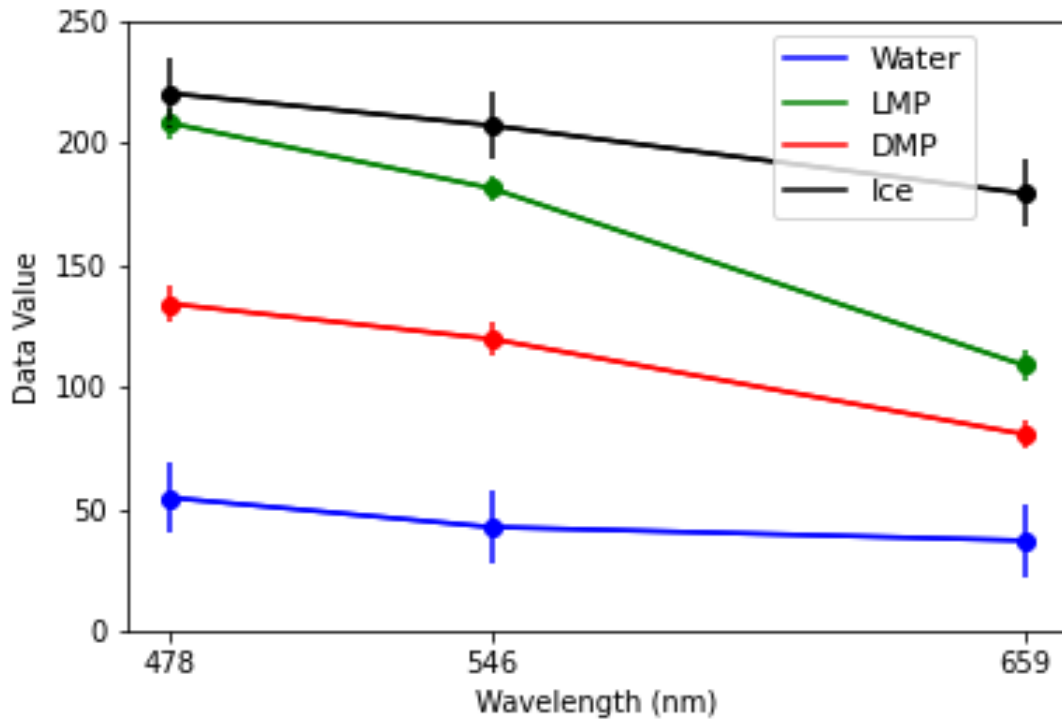ROIs had to be defined for each individual scene.

Figure 3: Training Spectra. Example of typical training data used by the MLC. Mean data

values (8-bit digital numbers) from each channel collected from training patches (ROIs) defined

for an image on June 27th, 2018. Error bars represent one standard deviation. Wavelengths

represent central wavelengths for each band (RGB).

Classification results from each tile were combined to retrieve total areal coverage of each class in the scene. Proportional coverage for each class was calculated by correcting for total number of pixels in the scene (sum of all classes, not including NaN pixels).

$$\text{Class Fraction} = \frac{\#\ of\ Pixels\ in\ Class\ of\ Interest}{LMP + DMP + Ice + Water} \qquad \textit{Equation 1.}$$

Pond fraction for an entire scene (f_{ps}) was calculated by taking the sum of pixels classified as LMP and DMP and normalizing that value to the total number of pixels in the scene (not including NaN pixels):

$$\text{Pond Fraction } (f_{ps}) = \frac{LMP + DMP}{LMP + DMP + Ice + Water} \qquad \textit{Equation 2.}$$

Pond fraction as a proportion of the ice (f_{pi}), rather than the entire scene, was calculated by removing water pixels and normalizing LMP and DMP to just the ice related classes:

$$\text{Pond Fraction } (f_{pi}) = \frac{LMP + DMP}{LMP + DMP + Ice} \qquad \textit{Equation 3.}$$

Representing pond fraction in two ways allows for melt pond data shown here to be quickly compared to any other study, regardless of how pond fraction was calculated. Additionally, f_{ps} is required to estimate energy flux to the ocean, whereas f_{pi} is more useful for considering pond growth on ice.

Some days had multiple scenes. If the scenes were adjacent, they were analyzed as one large scene. This was often the product of Maxar separating an elongated scene into two smaller

scenes for file size purposes. This accounts for some apparent variability in scene size (Table 1), which does not carry over into class area once it is normalized to total scene area. If multiple scenes from the same day were available but not adjacent, they were analyzed separately. All scenes, whether adjacent or not, were trained on their own set of ROIs.

Validation of Classification Accuracy

Machine classified pixels were compared at random with manual interpretation of their corresponding unclassified pixels, as there was no in-situ ground truth data for the images. Google's random number generator was first used to select a classified tile from each image. Using the geoprocessing tool "Create Accuracy Assessment Points" within ArcGIS Pro, a random sample of 100 pixels (25 for each class) was generated for each tile. These points were generated from the classified image but overlaid onto the unclassified image. All 100 points were then manually classified based on visual interpretation of the unclassified image. Results of this analysis were presented in confusion matrices (tables allowing visualization of classification performance) of the machine vs. manual classifications.

Spatial Characteristics of Individual Melt Ponds

Three classified images were selected for spatial analysis of individual melt ponds- June 18th, June 28th, and July 20th. Fragstats software (McGarigal et al., 2012) was employed to obtain a distribution of patch sizes for each date. A patch refers to a grouping of adjacent pixels of one class that are encompassed by pixels of other classes.

A random number generator selected a single tile from each date to be used for spatial analysis, as processing the entire scene would have exceeded the computational and temporal

resources available. WV imagery was re-projected to ESPG 32632 to satisfy Fragstats file input requirements. All image tiles exceeded the Fragstats maximum size limit for inputs (Fragstats is limited to using 2GB of memory), so qGIS software was used to split the selected tile from each scene into 10,000 by 10,000 pixel sub-tiles. Of the generated sub-tiles, the sub-tile that visually appeared to have the greatest number of FYI melt ponds was selected. The primary aim of conducting spatial analysis was to examine individual melt pond surface areas on FYI, so sub-tiles with large patches of open water or MYI flows were discarded.

These methods eliminate user bias up until the final step, for which manually selecting the sub-tile that accurately represented only FYI flows with no large patches of open water was essential for ensuring a large sample size and producing comparable data (i.e., pond density). In most cases there was an obvious sub-tile that best met this criterion, but if multiple sub-tiles appeared suitable, a random number generator was once again used to select the sub-tile for subsequent analysis. Outputs from Fragstats were presented in hectares, which was converted to square meters by multiplying each patch size by 10,000.

Patches smaller than 2 m^2 were removed. This threshold was adopted from Perovich et al. (2002b), who calculated median pond size from aerial imagery with similar spatial resolution. This threshold was also an accurate representation of the smallest ponds in the WV images that could be positively identified. Dropping the smallest patches is necessary for analysis, as there are numerous misclassified small patches spread throughout the image. These patches are minute enough (often 1 pixel) that they don't impact the overall interpretation of the image classification, but abundant enough that they skew median melt pond size towards 0 and yield unrealistically high pond densities if no threshold is in place. The impact of where the threshold is set is shown in Figure 4. Median surface area values increase linearly, with values roughly 2 –

2.5 times the size of the chosen threshold. Pond density estimates decrease by an order of magnitude with even a 2 m^2 threshold in place.
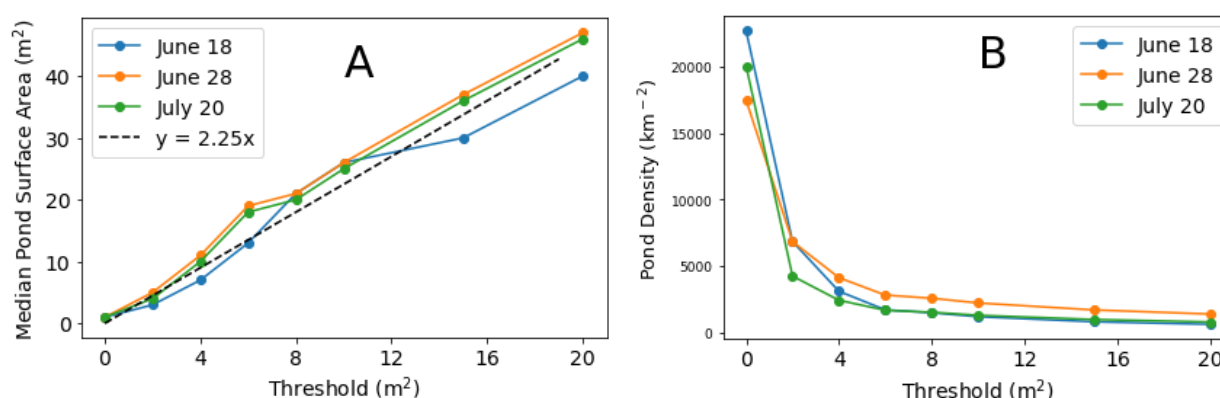
Figure 4: Melt Pond Size Threshold. Median pond surface area (A) and pond density (B) shown as functions of the threshold set for minimum acceptable pond size.

Development of Light Availability Data Product

A light budget for the surface of the water column across an entire scene was estimated using the relative areal coverage of each class in an image (Equation 4). $E_d(0^-)$ (mol m^{-2} d^{-1}) was the daily average downwelling irradiance over an entire classified scene, as seen just below the ice-water or air-water interface. C is the spatial coverage of a class, expressed as a proportion of the total scene area. The transmittance (τ), or proportion of surface irradiance transmitted below the water surface through a given surface condition for each class, is provided in Table 2. Transmittance varies with wavelength, and drops to 0 in the infrared, thus the large range of values. Transmittances representing "middle of the road" values for visible light were selected

and are shown in the far-right column. Note that ice and pond transmission increase with time to account for the melting of snow, and eventual thinning of the ice, as well as the deepening of ponds. Incident surface irradiance (in-air) from 400-700 nm (E_{PAR}) was obtained from instrument packages deployed on the surface of the ice measuring PAR (Photosynthetically Available Radiation) and air temperature (AT) (described below in *In-Situ Data* section).

$$E_d(0^-) = E_{PAR}[(C_{ice} \ \tau_{ice}) + (C_{water} \ \tau_{water}) + (C_{lmp} \ \tau_{lmp}) + (C_{dmp} \ \tau_{dmp})] \qquad \textit{Equation 4.}$$

Table 2: Transmittance Values Obtained from Previous Studies.

Class	Transmittance (τ)	Source	Chosen Value
Ice	0 – 0.034	Frey et al, 2011	0.01 (June 1st – June 5th)
	0 – 0.3	Light et al, 2015	0.05 (June 18th – June 28th)
	0 – 0.17	Light 2008	0.1 (July 13th – July 20th)
	0 – 0.073	Perovich 1998a&b	
Melt Pond	0 – 0.46	Frey et al, 2011	0.2 (LMP)
	0 – 0.73	Light et al, 2015	0.4 (DMP) (June 1st - 5th)
	0 – 0.4	Light 2008	0.5 (DMP) (June 18th - 28th)
	0.47 – 0.59	Arrigo et al, 2014	0.6 (DMP) (July 13th - 20th)
Water	0.98	Kirk, 1994	0.98

To evaluate the advantages of using high resolution imagery for estimating light availability, results were compared with those derived from the standard National Snow and Ice Data Center (NSIDC) Sea Ice Concentration product. These data were available as part of the

NSIDC Sea Ice Index dataset (Version 3) and have a spatial resolution of 25km (Fetterer et al., 2017). Data were downloaded as GeoTiffs, and analyzed in ArcGIS Pro. Ice concentration for pixels within the extent of the WV images were recorded from the NSIDC image. If a WV image overlapped across multiple NSIDC pixels, an average value of those pixels was taken. Any part of the NSIDC pixels not classified as ice was considered open water. Light availability was calculated using Equation 5, in line with existing light penetration indices (Pinkerton & Hayward, 2021). Melt ponds are not included as a class, as they are not retrievable in the NSIDC imagery.

$$E_d(0^-) = E_{PAR}[(C_{ice} \ \tau_{ice}) + (C_{water} \ \tau_{water})] \qquad \textit{Equation 5.}$$

Light Driven Primary Production Under the Ice

A model described in Hill et al. (2018) was used to further explore relationships between light availability and potential primary production. Equation 6 is adapted from Hill et al. (2018) and shows the calculation of net biomass specific production (P_{net}^B). Terms inside the curly brackets calculate gross biomass-specific photosynthesis, which after the subtraction of respiration (R^B) yields P_{net}^B.

$$P_{net}^B = \left\{ P_E^B \left[1 - exp\left(\frac{-\emptyset_m * A_\emptyset^*(\lambda) * [Chl\ a] * E_d 0^-(\lambda, t)}{P_E^B} \right) \right] \right\} - R^B \qquad \textit{Equation 6.}$$

The model was run for a 24-hour period in 1-hour timesteps using a downwelling irradiance spectrum from June 1st [$E_d(\lambda, t, z_{0+})$], propagated to a single depth bin located just beneath the ice-water interface [$E_d 0^- (\lambda, t)$]. Model runs were repeated several times, with each

run transmitting a different fraction of downwelling surface irradiance to the ice-water interface

to represent various levels of light transmission through the ice pack. The model results allow

for the generation of a simple photosynthesis vs. irradiance curve that can then be related to melt

pond coverage. A water temperature of -1°C, replete nutrients, and no grazing were assumed.

Additional constants are defined in Table 3.

Table 3: Conditions for Model Runs.

Symbol	Definition	Value	Dimensions	Source
$E_d(\lambda,t,z_{0+})$	Incident downwelling irradiance spectrum at the ice surface	Function of (λ)	μmol m^{-2} s^{-1}	Modeled using Hydrolight ©
$E_d0\ (\lambda,t)$	downwelling irradiance spectrum at the ice water interface	Function of (λ)	μmol m^{-2} s^{-1}	Calculated using a varying ice transmission coefficient
[Chl a]	Chlorophyll a concentration	1	mg m^{-3}	Set to initial value in model
P_E^B	Biomass-specific rate of light-saturated photosynthesis	0.11	mmol C mg Chl^{-1} hr-^{1}	Platt et al., 1982
Φ_m	Quantum yield of photosynthesis (Carbon) for absorbed photons	0.104	mol C fixed mol photons absorbed^{-1}	Hill et al., 2018
Aϕ*(λ)	Spectral absorptance	Function of λ	Dimensionless	Hill, 2004
P_{net}^B	Net biomass-specific photosynthesis	Calculated in model	mg C mg Chl^{-1} hr^{-1}	Equation 6
R^B	Biomass-specific respiration	5% of P_E^B	mg C mg Chl^{-1} hr-^{1}	Forest et al., 2011

In-Situ Data

WARM (Warming and Irradiance Measurements) Buoys (WB) and their associated sidekicks (SK) provide in-situ data co-located with WV imagery (Figure 5). These data are available at the NSF Arctic Archive (Hill, 2019), and full technical details can be found in Hill et al (2018). Data from WB7 & 8, and sidekicks 3 & 4 (SK3 & SK4, co-deployed respectively) were collected at hourly time intervals, beginning March 30th, 2018, and designated in GMT. Measured variables used in this study included sea surface temperature (SST, ^{o} C) from WB7 and WB8, air temperature (^{o} C) from SK3 and SK4, and surface irradiance (PAR, µmol m^{-2} s^{-1}) incident on the ice from all platforms. Figure 5 shows deployment orientation of the sensors.

Air temperature (AT) and incident irradiance from 400-700 nm (PAR) from both buoy locations was required for analysis of environmental variables driving melt pond formation. The AT data from SK 3 & 4 at 0.5 m above the ice surface represented true air temperature, while SST on the buoy, due to orientation, represented an ice-air interface temperature, with observed values generally lower than that of the SK AT. Unfortunately, SK3 fell over on June 9th due to surface ice melt, and no longer produced usable data. The average offset between AT and SST (ice-air interface temperature) between May 1st and June 8th was 3.94 degrees. This correction was applied to the WB7 SST measurement to provide a proxy for AT after the failure of SK3 (Figure 6A).
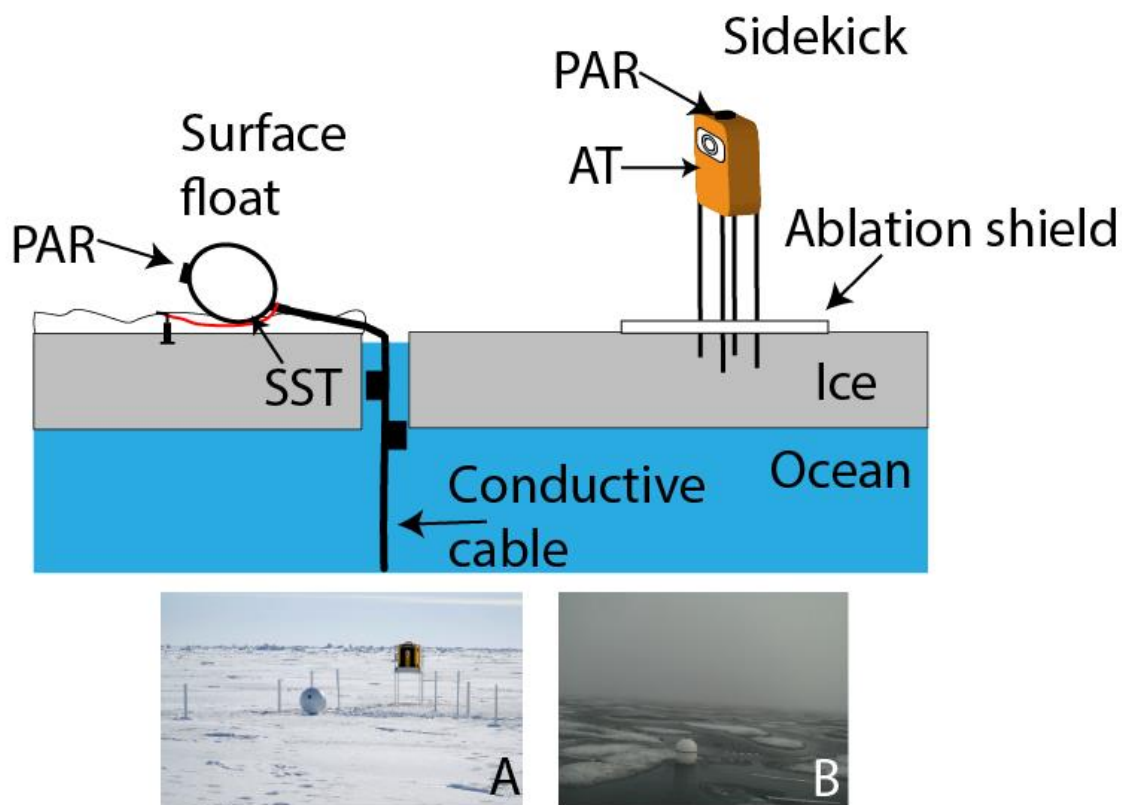
Figure 5: WARM Buoy and Sidekick Design. Orange box represents the SK instrument, and the white circle (left) represents the surface float of the WB. Downwelling PAR sensors and thermistors are labeled. The buoy rests in a sideways orientation on the ice, before being pulled down by the tether and into an upright position as the ice melts. A. Photograph of WB and SK taken after deployment on March 30th 2018. B. Photograph taken by SK of heavily ponded surface on July 3rd 2018.

Similarly, PAR was measured on the top of the sidekicks and was used until SK3 tipped over. The radiometers on the buoys initially face 90 degrees from the ice surface, as the buoys

lay sideways on the ice until they melt out, at which point they float in an upright position and begin measuring true downwelling irradiance. PAR measured by the SK is generally higher than that measured by the buoy while in its initial deployment orientation. A correction factor of $+ 4.6$ mol m^{-2} d^{-1} was used to correct the WB7 PAR to that expected from SK3 (Figure 6B). No corrections were needed for SK4, as it remained in the vertical orientation on the ice for the duration of its coincident WV imagery.
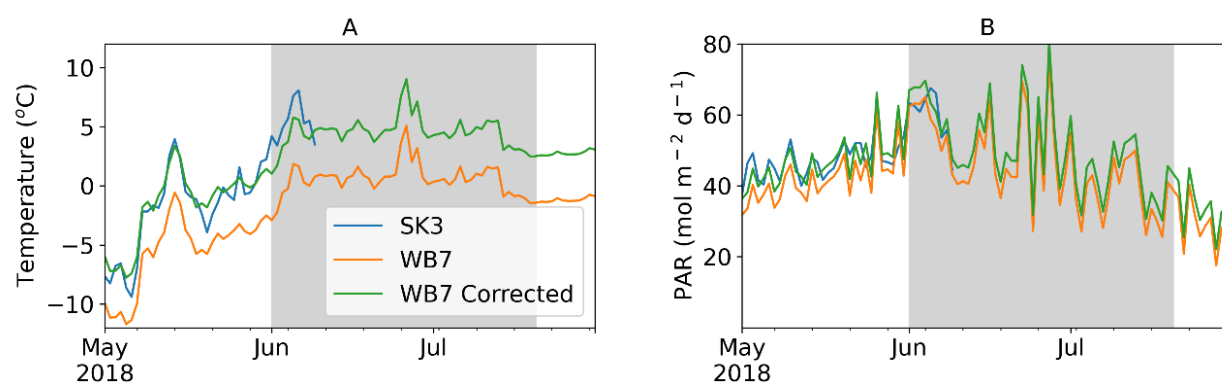

Figure 6: Daily Average In-Situ Data. Shaded regions denote the time-period from which WV imagery was analyzed. A. Daily temperature from WB7 and SK3, and WB7 temperature after application of correction factor ($+3.94$ $^{\circ}$C). B. Daily PAR at WB7 and SK3, and WB7 PAR after application of correction factor ($+4.6$ mol m^{-2} d^{-1}).

RESULTS

Classification Accuracy

Figure 7 is a visual representation of a typical classification. Large patches of open water were identified and separated from ice flows. Melt ponds were clearly defined, while still preserving the snow and ice ridges in between. There are also noticeable differences in both visual appearance and predominating pond type between FYI and MYI. Note that MYI (denoted by black box) is comprised primarily of LMP, while FYI is dominated by DMP.

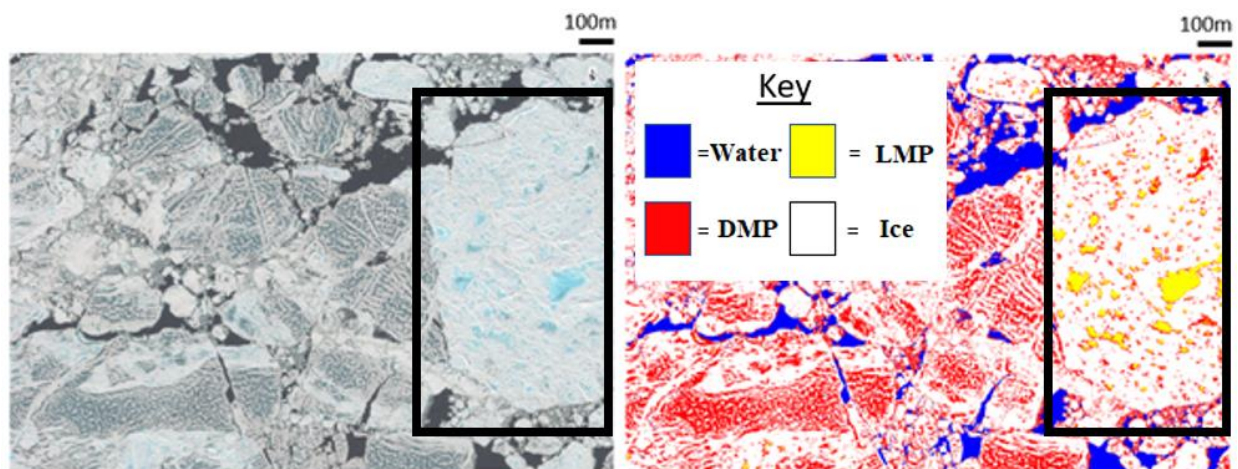**Figure 7: Classification Example.** Comparison of an unclassified (left) and classified (right) WV-2 image from June 28th, 2018. 4 classes are shown here: open water (blue), ice (white), light melt pond (LMP) (yellow), and dark melt pond (DMP) (red). An MYI ice flow is highlighted by the black box. This figure depicts a fraction of a larger tile and is not indicative of the class distribution for the entire scene.

Figure 8 displays classification U-scores ("User Score", or reliability score) for each class, as well as the fraction of the image that class accounts for as a function of time. The U-score shows the fraction of randomly selected points for a given class that the user confirmed as being correctly classified. For example, a DMP U-score of 0.8 results from the user confirming 80% of the pixels that the algorithm classified as DMP during manual pixel-by-pixel verification. U-scores say nothing about what the true classification of the other 20% (false positives) of pixels were. Low U-scores indicate over-estimation of that class by the MLC. Water and ice (8A & 8B) were classified accurately for the entire time series, with scores almost always > 0.9. Melt pond classification accuracy improved as the summer progressed and ponds increased and became more defined, with the greatest degree of misclassification in the earliest scenes when pond fraction was very low, resulting in minimal over-estimation (8C & 8D).
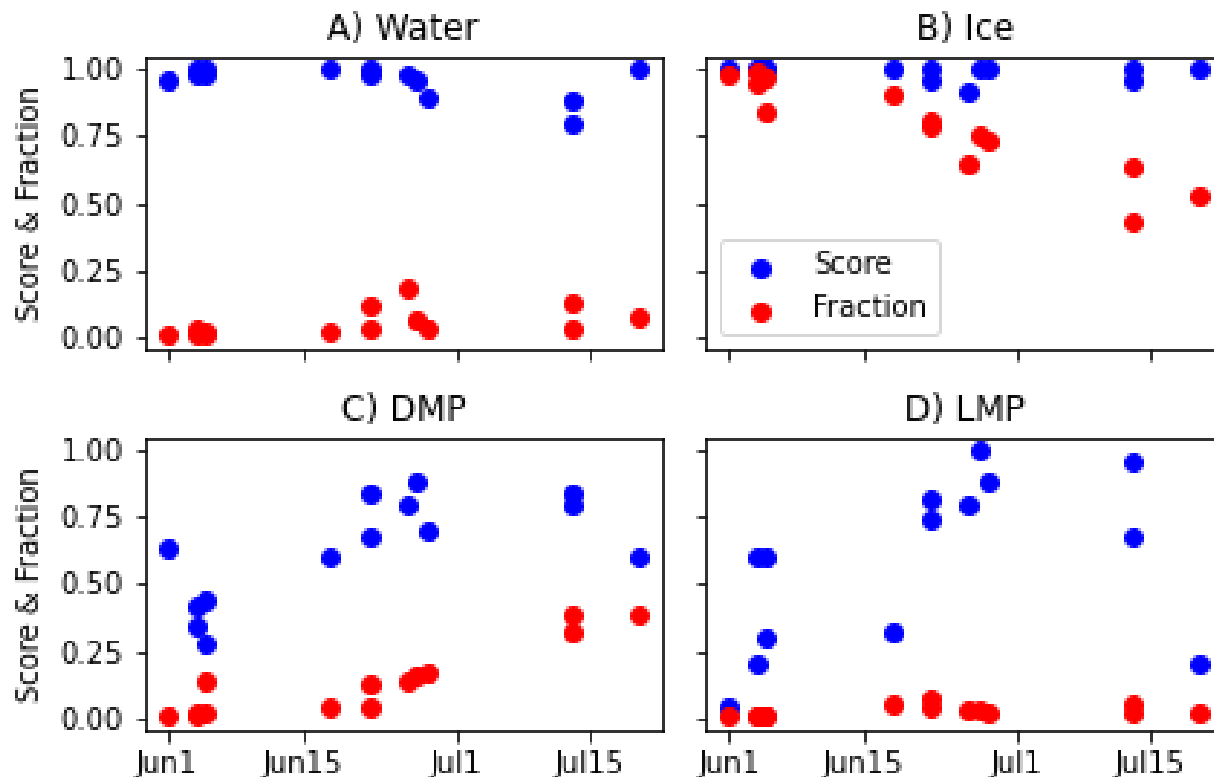
Figure 8: Summary of U-Scores. U-Scores reflect the accuracy of machine classified pixels in reference to user classified pixels. The lower the U-Score, the more over-estimation of that class occurred in the classification. Fraction refers to the total areal coverage of each class normalized to the total area of the image (Equation 1).

Classification P-scores ("Producer Score") quantify false negatives for a class (where manually classified pixels were classified as something else by the MLC). Low P-scores thus indicate underestimation of that class by the automated classifier. For example, a P-score of 1 for LMP demonstrates perfect agreement between the manual classification and MLC.
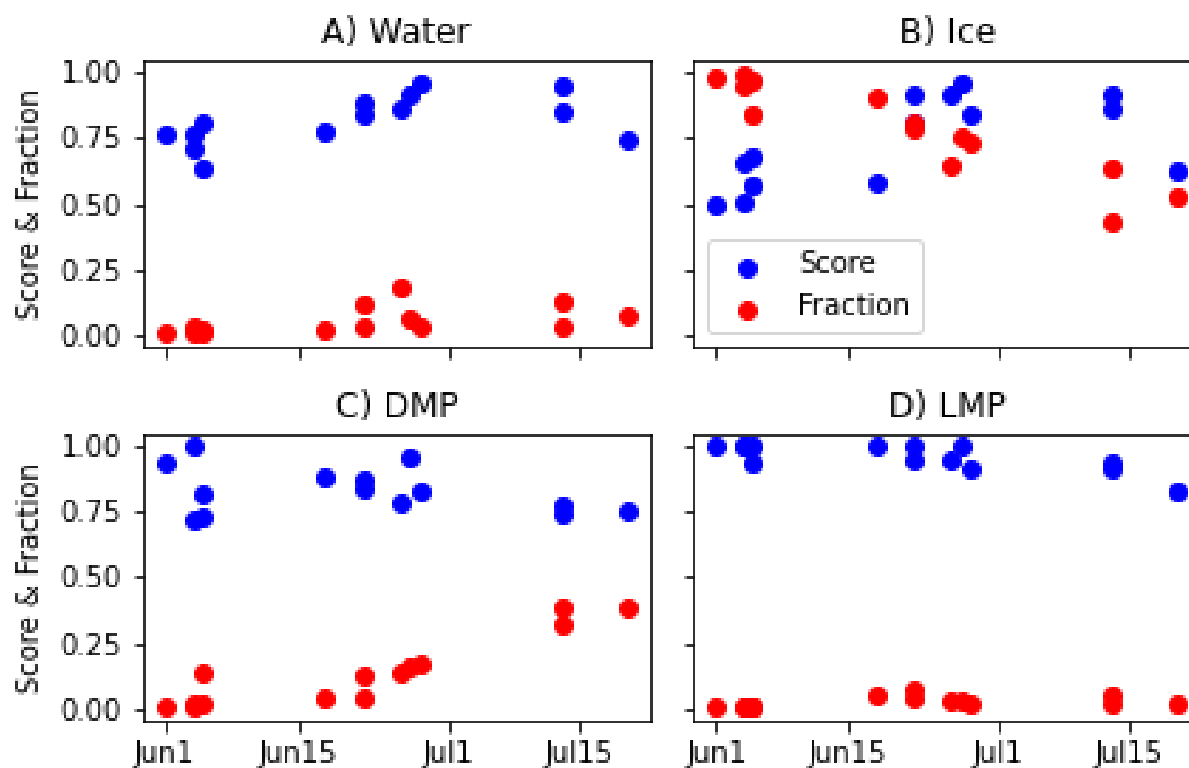
Figure 9: Summary of P-Scores. The P-score quantifies false negatives for a given class (the algorithms performance in reference to the user performed manual verification). A low P-score implies underestimation of that class by the MLC. Fraction refers to the total areal coverage of each class normalized to the total area of the image (Equation 1).

Water P-scores consistently above 0.75 indicate that other classes were not often misclassified as water, though some underestimation of the water class does exist (Figure 9A), such as when ice draft (submerged edge of an ice flow) was misclassified as DMP (Figure 10A). Ice was more variable at the beginning of the time series during its highest concentration (Figure 9B), when it contained various features that were likely to be mis-identified, including blue-colored snow ridges (Figure 10B), the shading associated with snow ridges, (Figure 10C) and

recently refrozen leads classified as DMP (Figure 10D). These misclassifications lead to a P-score of ~ 0.5 in early June when un-ponded ice dominated the images, causing the areal extent of ice cover to be underestimated (Figure 9B).   The P-score for ice increased as ice ridges and re-frozen leads disappeared at the end of June and into July.

LMP and DMP have P-scores > 0.5 throughout the summer (Figure 9C & 9D). Some very dark melt ponds were misclassified as open water (Figure 10E), but the overall classification accuracy of individual DMPs was high. Over 97% of pixels in visually examined melt ponds were correctly identified, demonstrating that though other features may be getting misclassified as ponds, melt ponds themselves are not being missed by the classification (Figure 11). More detailed descriptions of u-scores and p-scores can be found in Olofsson et al. (2013).
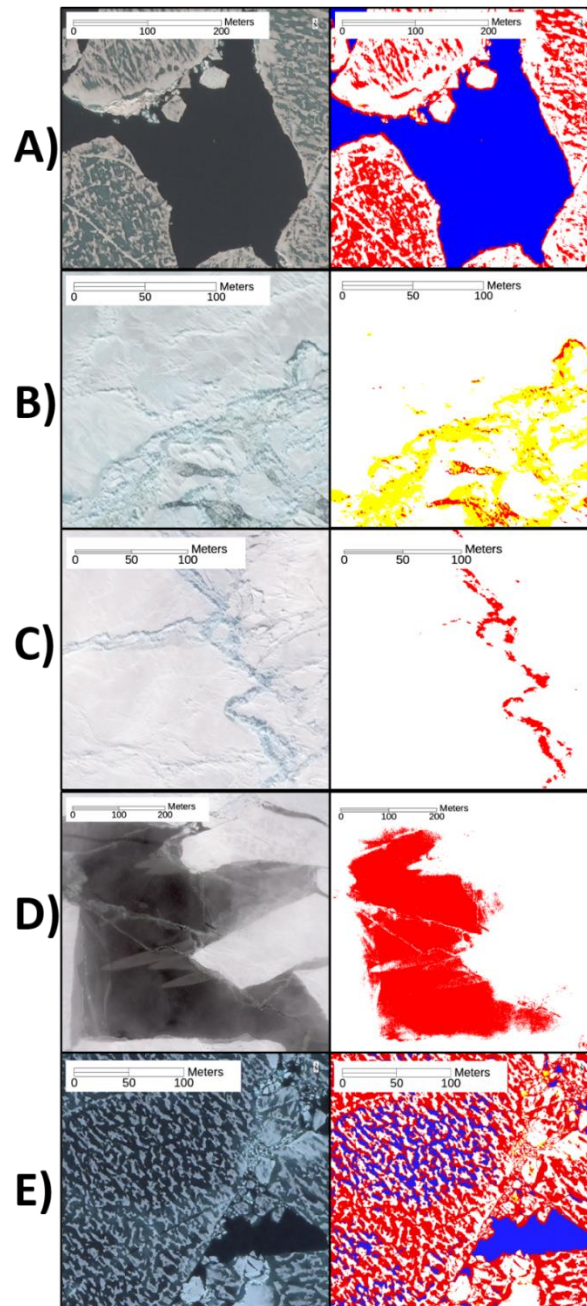
Figure 10: Common Misclassifications. A. Very dark ponds (red) partially misclassified as water (blue). B. Snow ridge pixels misclassified as LMP (yellow). C. Snow ridge shadow misclassified as DMP (red pixels). D. Very thin ice misclassified as DMP (red). E. Ice draft (edge) misclassified as DMP.
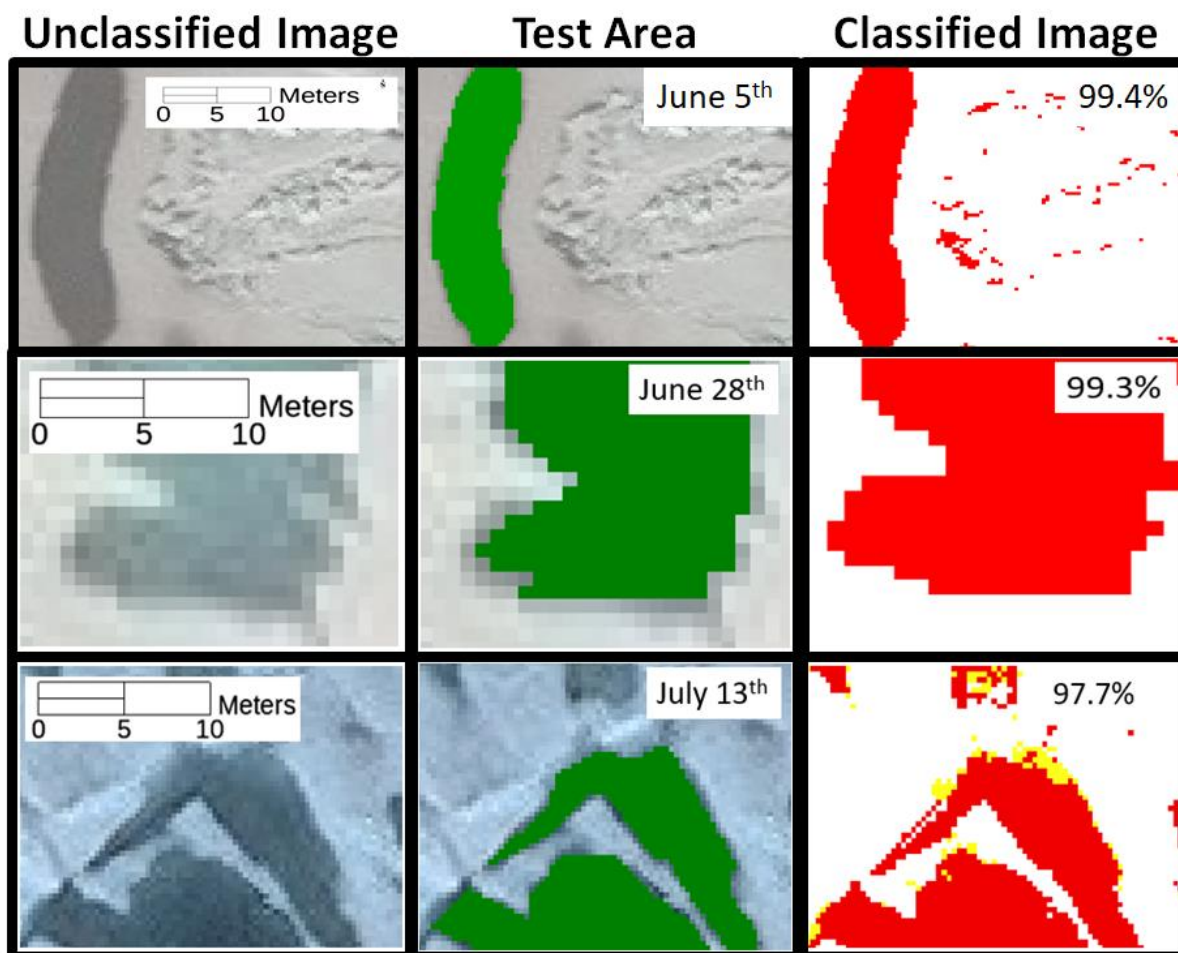
Figure 11: Melt Pond Classification Accuracy. 3 images of melt ponds from June 5th, June 28th, and July 13th (top to bottom, respectively) (left). User-defined polygons in green to serve as test areas (center). Classified images (right). Values in the top right corners indicate the percentage of test area pixels correctly classified as DMP. Red pixels signify those classified as DMP, yellow pixels were classified as LMP, and white pixels were classified as ice.

Class Distribution Data

Analysis of satellite imagery began on June 1st, 2018, when >98% of the imagery was comprised of un-ponded sea ice (which will be referred to as "ice" for the remainder of the text).

The 2-dimensional coverage of ice decreased as the summer progressed, being replaced by an increasing proportion of DMP, which approached a fraction of 0.4 by late July (Figure 12). Open water and LMP made up small fractions of the overall scenes. The June 26th image was marked by the highest concentration of open water for the entire time series (0.18). Subsequent imagery on June 27th showed an increase in ice and decrease in water, followed by a resumption of the long-term trend of decreasing ice.
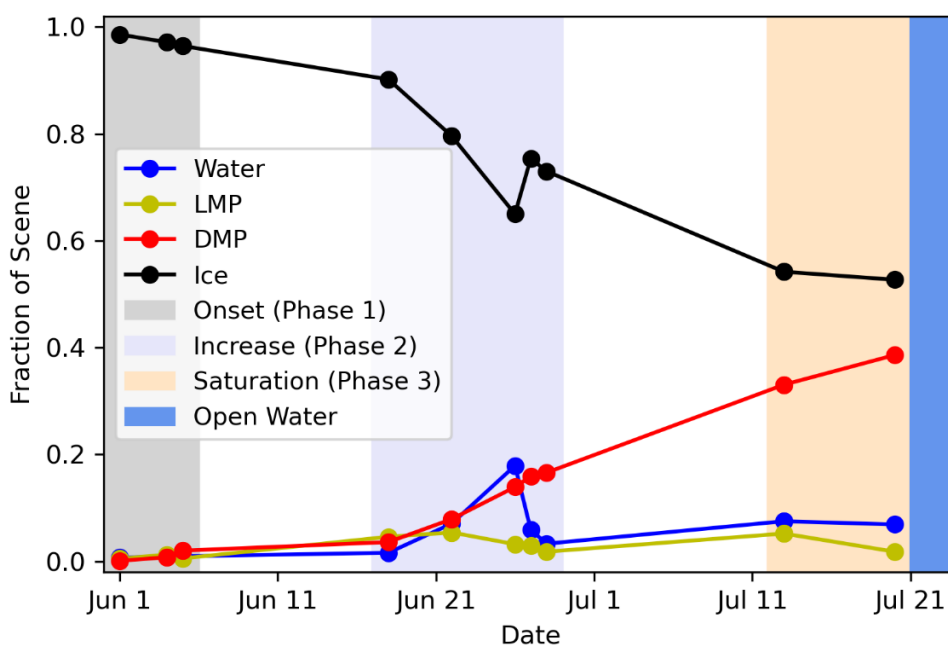
Figure 12: Time Series of Class Abundance. Only one data point is shown per day, reflecting the average class fraction for that day from all scenes, even if they were not adjacent. Data collection ended on July 20th, as subsequent imagery contained large fractions of open water accompanied by unclassifiable ice rubble. See text for further descriptions of phases.

Three distinct phases of DMP evolution on sea ice were observed both qualitatively and quantitatively- those being onset (Phase 1), increase (Phase 2), and saturation (Phase 3). All phases are depicted graphically in Figure 12, and visually in Figures 13, 14 & 15. Phases are only defined for periods in which imagery was available. The onset phase (June 1st – 5th), represented the first observations of melt ponds, and was characterized by few ponds clustered in small groupings, with >90% of the images being composed of ice, some of which was still snow covered (Figure 13). Both open and recently re-frozen leads can be observed. The light/dark pattern observable in the June 1st image showed a network of bare ice patches that were separated by snow dunes (Figure 13A). Though pond fraction was low in this phase, melt ponds appeared in small clusters as seen in a snapshot from June 4th (Figure 13B).
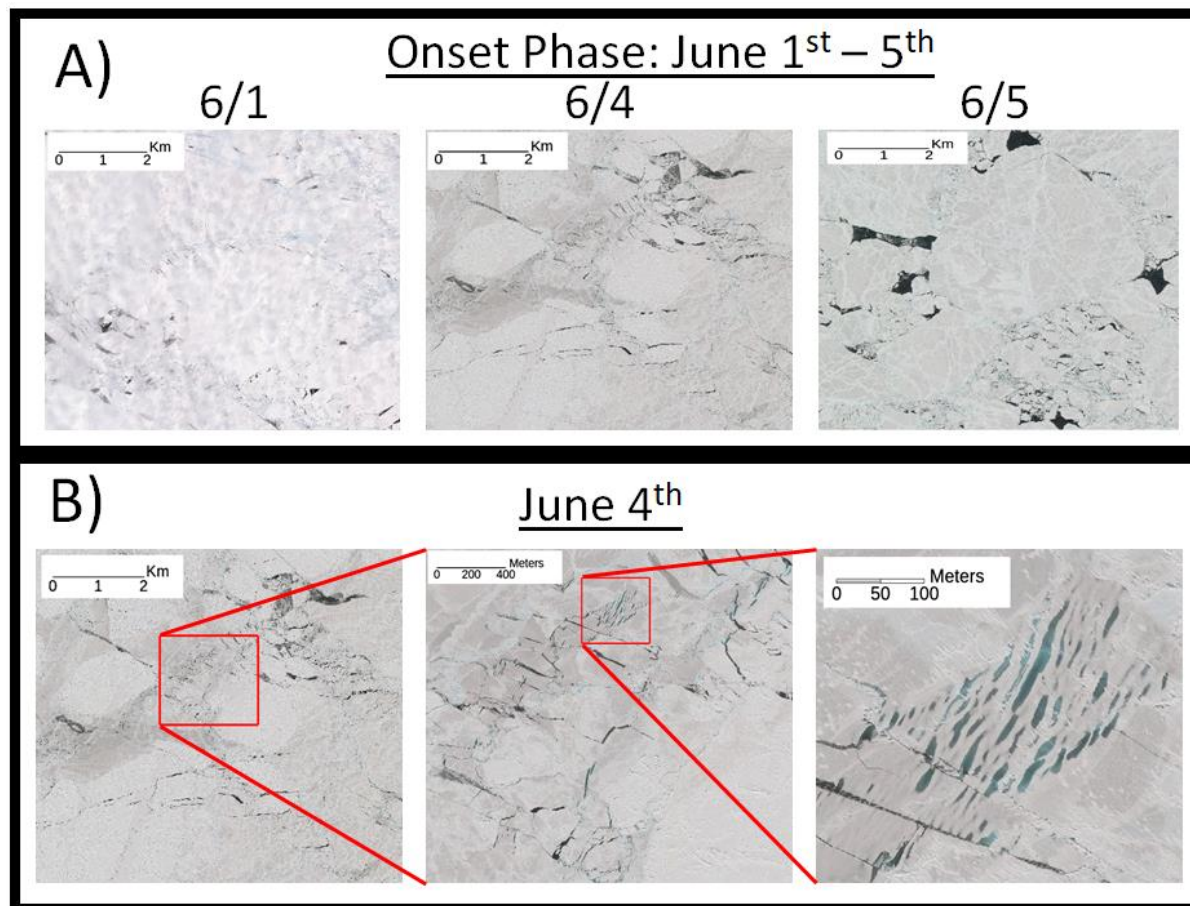
Figure 13: Onset of Ponding (Phase 1). A. Selections of scenes from June 1st, 4th and 5th. B. Sections of the image from June 4th at successive levels of magnification highlighting typical appearance of melt ponds for this phase.

The increase phase (June 18th – 28th) marks a shift in which the ice quickly became covered in ponds, and the DMP fraction increased from 0.04 on June 18th to 0.17 on June 28th (Figure 12). Images from late June showed a clear darkening in the ice caused by pond presence, though the ice remained mostly intact, and ponds were still visually brighter than the surrounding patches of open water (Figure 14A). By June 22nd, pond coverage visually increased as ponds

began to cover large portions of the ice. Ponds were distinct, still had a bluish color, and were generally surrounded by ice (Figure 14B).
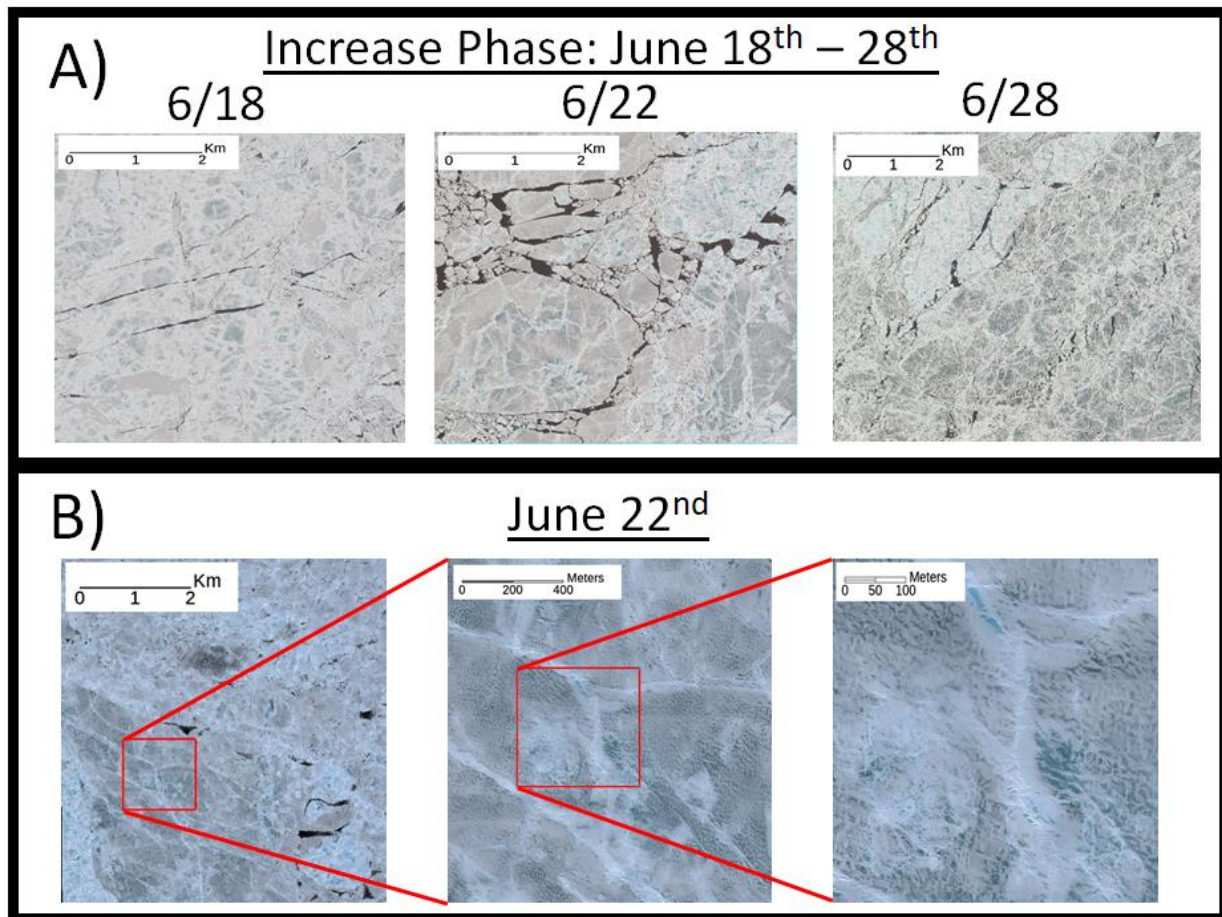
Figure 14: Ponding Increases (Phase 2). A. Selections of scenes from June 18th, 22nd and 28th. B. Sections of the image from June 22nd at successive levels of magnification highlighting typical appearance of melt ponds for this phase.

The saturation phase (July 13th – 20th) showed ice flows that were nearly flooded with many interconnected ponds (Figure 15A). By July 13th ponds had darkened significantly, suggesting they may have deepened. By July 20th, ponds became nearly as dark as the open water (Figure 15B). DMP fraction reached its maximum recorded value, approaching 0.4 (Figure 12). By the end of the saturation phase, ice appeared to be disintegrating, as the heavy concentration of ponding had compromised the structural integrity of the ice pack.
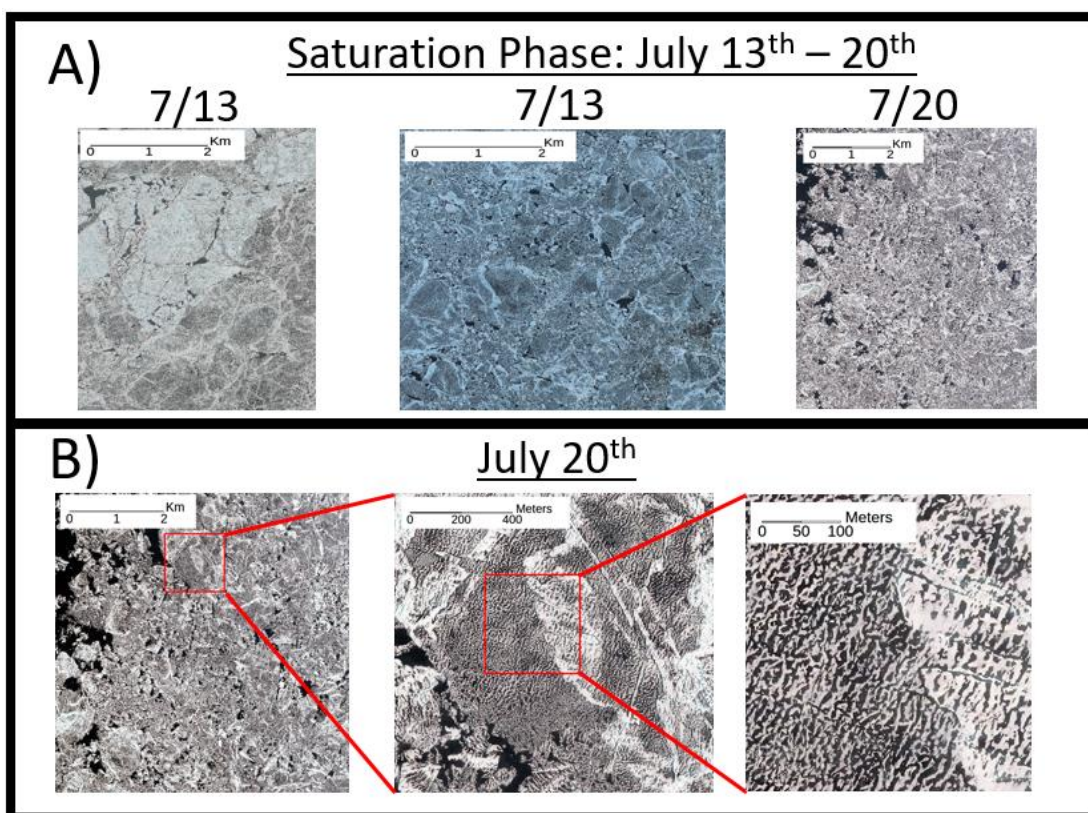
Figure 15: Pond Saturation of Ice Flows (Phase 3). A. Selections of scenes from July 13th and 20th. B. Sections of the image from July 20th at successive levels of magnification highlighting typical appearance of melt ponds for this phase.

Finally, images from July 21st show scenes that were mostly open water, with the remaining ice rapidly disintegrating (Figure 16). Images after July 20th were not available as Pan-Sharpened RGB's and were thus unclassifiable.
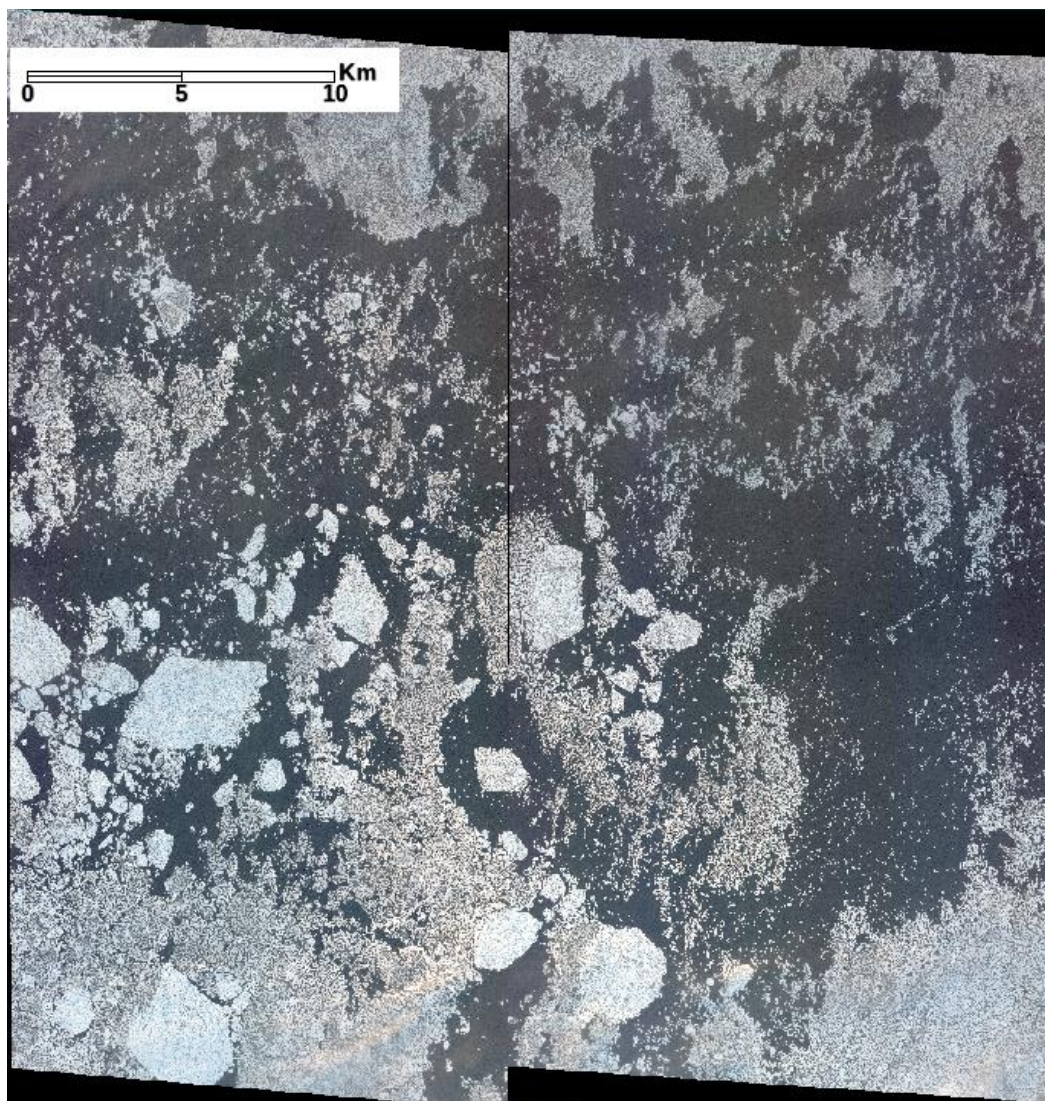
Figure 16: Disintegration of Ice Pack. 2 Stock images (not pan-sharpened) from July 21st, 2018. Upper left extent: 72.90N, 163.09W. Lower right extent: 72.61N, 162.05W.

Environmental Drivers of Melt Pond Growth

Data from in situ instrumentation on WB7/SK3, and WB8/SK4 were similar despite their spatial separation (Figure 1). Daily air temperature was below -7° C at the start of May, increased to above 0° C briefly in mid-May, but quickly fell back below freezing (Figure 17A). By the start of June, air temperature was consistently above freezing, with an average daily air temperature of approximately 5° C, with daily variation of ±1.5° C throughout June and July. Daily PAR at the start of May was approximately 37 mol m^{-2} d^{-1} with some daily variation of ± 5 mol m^{-2} d^{-1} throughout May (Figure 17B). At the start of June, daily PAR reached a high of ~ 67 mol m^{-2} d^{-1}. Day to day variation was high throughout June and July (~ 11 mol m^{-2} d^{-1}) with an overall decreasing trend in daily irradiance (Figure 17B).
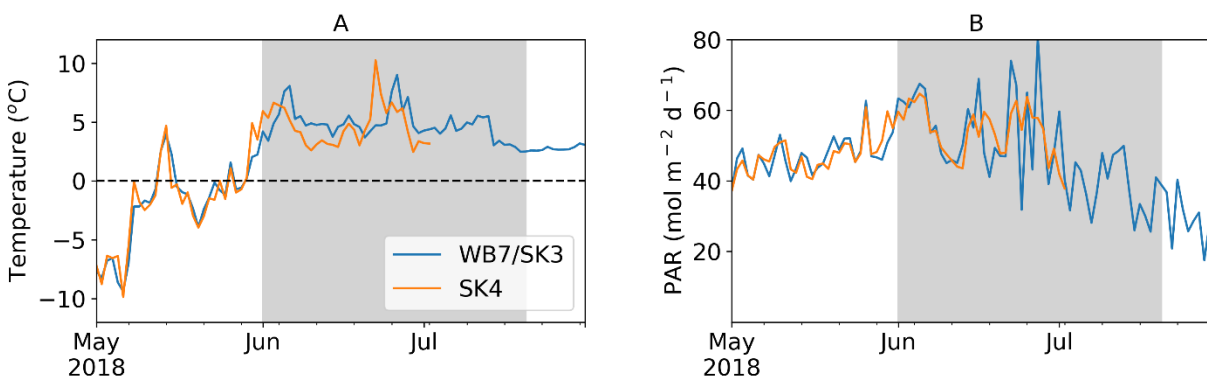
Figure 17: In-Situ Data. Corrected WB7/SK3 (see methods section) and original SK4 data. A. Daily average air temperature with dashed line representing 0° C. B. Daily PAR. Shaded section denotes the time period from which WV imagery was used.

Pond fraction was regressed against these in situ environmental variables to search for strong predictors. Mean daily values of air temperature and incident PAR were found to be poor predictors of melt pond development (Table 4), though PAR did have a significant relationship with pond fraction ($p < 0.01$). Cumulative hours above freezing (as measured above the surface) was found to be a strong predictor of pond fraction ($r^2 = 0.90$, $p < 0.01$). Hours above freezing (0° C) were counted beginning on May 28th (the first day in an instance of more than 3 days in a row that had daily average air temperature values above 0° C). No significant ponding or periods of prolonged temperatures above freezing were observed beforehand.

Table 4: Pond Fraction Relationships. Coefficients of determination and p-values between pond fraction (f_{ps}) and variables measured by the WARM buoys.

Variable	Units	Relationship Type	r^2	P-value
Mean Daily Surface PAR	μmol m^{-2} s^{-1}	Linear (negative)	0.38	*< 0.01*
Mean Daily Air Temperature	$^\circ$C	Linear (negative)	0.09	0.27
Cumulative Hours Above Freezing (AT)	Dimensionless	Linear (positive)	0.90	*< 0.01*
Cumulative Hours Above Freezing (AT)	Dimensionless	Logistic	0.96	*< 0.01*

A simple linear model where pond fraction grows at a rate of 3 x 10^{-4} hr^{-1} above freezing provides robust predictability of pond development for f_{ps} and f_{pi} ($r^2 = 0.90$ & 0.88 respectively, y-intercept forced through zero). A logistic growth model (Equation 7) was also strongly predictive ($r^2 = 0.96$ & 0.93 for f_{ps} and f_{pi} respectively) with less variability around all 3 phases, whereas the linear models overestimated pond fractions before 800 hr, and underestimated

values after 800 hr (Figure 18). Table 5 provides descriptions and values for the variables in

Equation 7.

$$Pond\ Fraction = \frac{a}{1+e^{-k(Hrs-b)}}$$

<div align="right">*Equation 7.*</div>

Table 5: Logistic Curve Variables. Chosen values for Equation 7 variables. The upper limits

of the curves (a) were defined by the highest values recorded in the respective data sets. The

midpoints (b) and initial slopes (k) were allowed to vary to achieve the best fit, while still

preserving the overall logistic growth shape.

Variable Name	Mathematical Description	Qualitative Description	Values
a	Upper Limit of Curve	Maximum Value Observed (dimensionless)	f_{ps}: 0.44 f_{pi}: 0.51
b	Midpoint of Curve	Point where Pond Formation Rate Begins to Decline (hr above freezing)	f_{ps}: 725 f_{pi}: 725
k	Logistic Growth Rate (Slope)	Solved for Using Known x and y (hr above freezing^{-1})	f_{ps}: $6.4 * 10^{-3}$ f_{pi}: $6.7 * 10^{-3}$
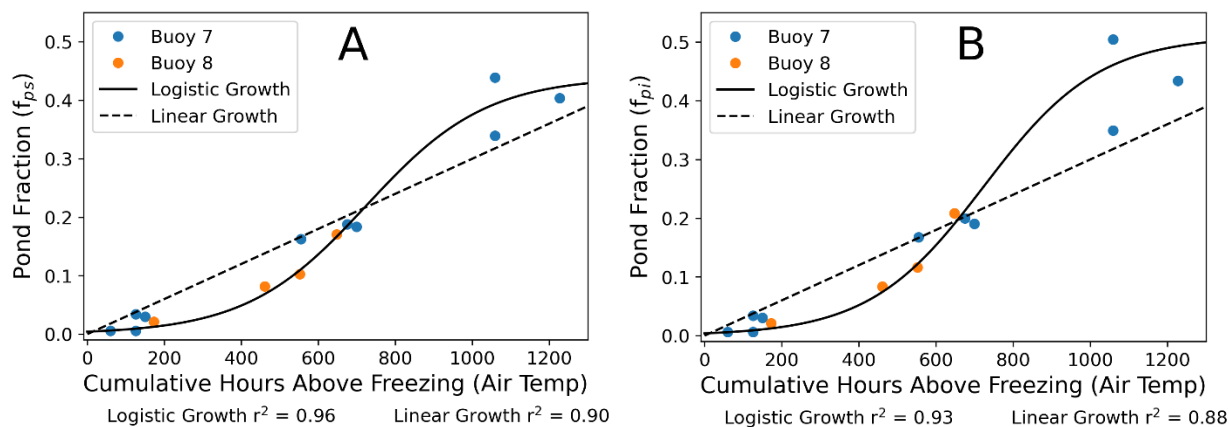
Figure 18: Melt Pond Growth Models. Linear and logistic growth models for melt pond (DMP + LMP) fraction as a function of cumulative hours above freezing. A. Pond fraction of the entire scene (f_{ps}). B. Pond fraction of only ice-covered area (f_{pi}).

Individual Melt Pond Size

      Images from three dates were selected for spatial analysis of pond size-frequency distribution. The dates were chosen from the beginning and end of the increase phase (June 18th & 28th, Figure 14), and the end of the saturation phase (July 20th, Figure 15) to provide a good snapshot of how pond shape and size changed through time. An onset phase image was not included, as there were very few ponds present. Melt pond size distributions were non-normally distributed across all images, with ponds smaller than 10 m^2 comprising more than 60% of the pond count, and ponds smaller than 1,000 m^2 making up >99% of the pond count across all three dates (Figure 19A). Median pond size was consistently small, although it did increase from 3 to 6 m^2 between June 18th and July 20th (Table 6). Pond density decreased as pond fraction increased and ponds became larger with nearly 3,000 fewer ponds km^{-2} on July 20th than on June 18th (Table 6).
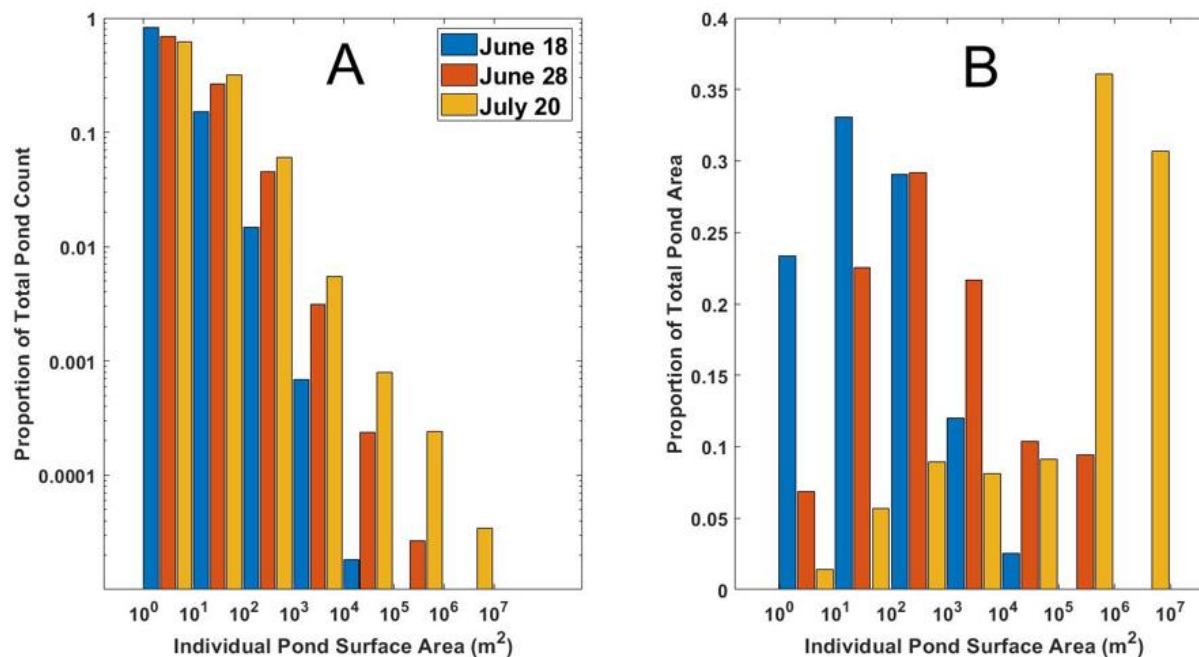
Figure 19: Melt Pond Size Histograms. A. Surface area size distributions normalized to total number of ponds for 3 separate dates. B. Pond size distribution for the same dates normalized to total pond surface area.

Table 6: Median Pond Sizes and Densities.

Date	Median Pond Size (m²)	Pond Density (ponds km⁻²)
June 18th	3	8,472
June 28th	4	6,190
July 20th	6	5,845

Despite their abundance, ponds smaller than 10 m^2 accounted for less than 25% of total pond area throughout the study period (Figure 19B). Total pond area on June 18th was primarily

dominated by small ponds, with >85% being made up of ponds <1,000 m^2. The frequency

distribution of pond area was gaussian-like (though still non-normal) on June 28th, as a wide

range of medium sized ponds (10 – 100,000 m^2) were responsible for >90% of total pond area.

Large ponds (>10,000 m^2) accounted for >80% of total pond area on July 20th, with only 8 ponds

accounting for ~65% of the area. One large pond of over 1,000,000 m^2, accounted for 30% of

the area (Table 7). These large, irregularly shaped ponds are produced by the fusion and

interconnection of individual ponds throughout the melting process (Figure 15B).

Table 7: Binned Pond Counts from Select Sub-Tiles.

Pond Size (m^2)	June 18th (# of ponds)	June 28th (# of ponds)	July 20th (# of ponds)
10^0 - 10^1	90,920	25,905	17,857
10^1 - 10^2	16,683	9,935	9,231
10^2 - 10^3	1,631	1,691	1,746
10^3 - 10^4	75	118	159
10^4 - 10^5	2	9	23
10^5 - 10^6	0	1	7
10^6 - 10^7	0	0	1

Modeled Light Availability

Both magnitude and proportion of surface irradiance (PAR) transmitted to $E_d(0^-)$ were

correlated with pond fraction ($r^2 = 0.90$ & 0.91, Figure 20A, 20B). The relationship between

$E_d(0^-)$ and melt pond fraction (Figure 20A) was used to estimate how phytoplankton growth

under the ice would be impacted by melt pond fraction (Figure 21) using the model adapted from

Hill et al. (2018). The resulting relationship followed a saturation-type response with respect to

daily PAR common to photosynthesis-dependent processes.
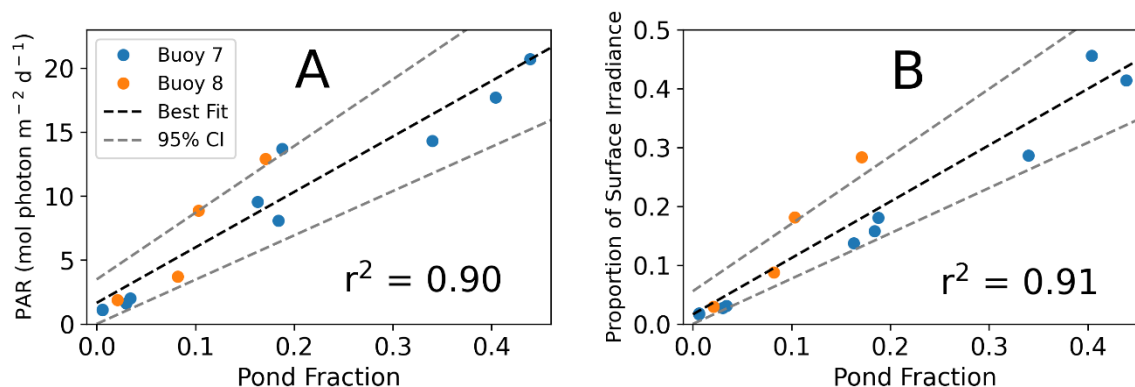
Figure 20: Modeled Irradiance. Photon flux (from buoy surface irradiance) (A) and proportion

of surface irradiance (B) calculated just below the water surface [$E_d(0^-)$] and averaged across the

scene. Data were regressed against pond fraction, and 95% confidence intervals are shown.

At the onset of melt pond development, small increases in pond fraction (and therefore

PAR) had a large impact on carbon uptake and chlorophyll growth (Figure 21). Chlorophyll *a*

(Chl *a*) growth rose from <1% d^{-1} to >34% d^{-1} as pond fraction increased from 0 to 0.05.

Correspondingly, carbon uptake increased from <0.1 mmol C $m^{-2} d^{-1}$, to nearly 0.86

mmol C $m^{-2} d^{-1}$. As pond fraction continued to increase, % Chl *a* growth reached a saturating

upper limit of ~60%, with carbon uptake saturating at ~1.3 mmol C m^{-2} d^{-1} for pond fractions

above 0.15 and daily PAR above 5 mol photons m^{-2} d^{-1}.
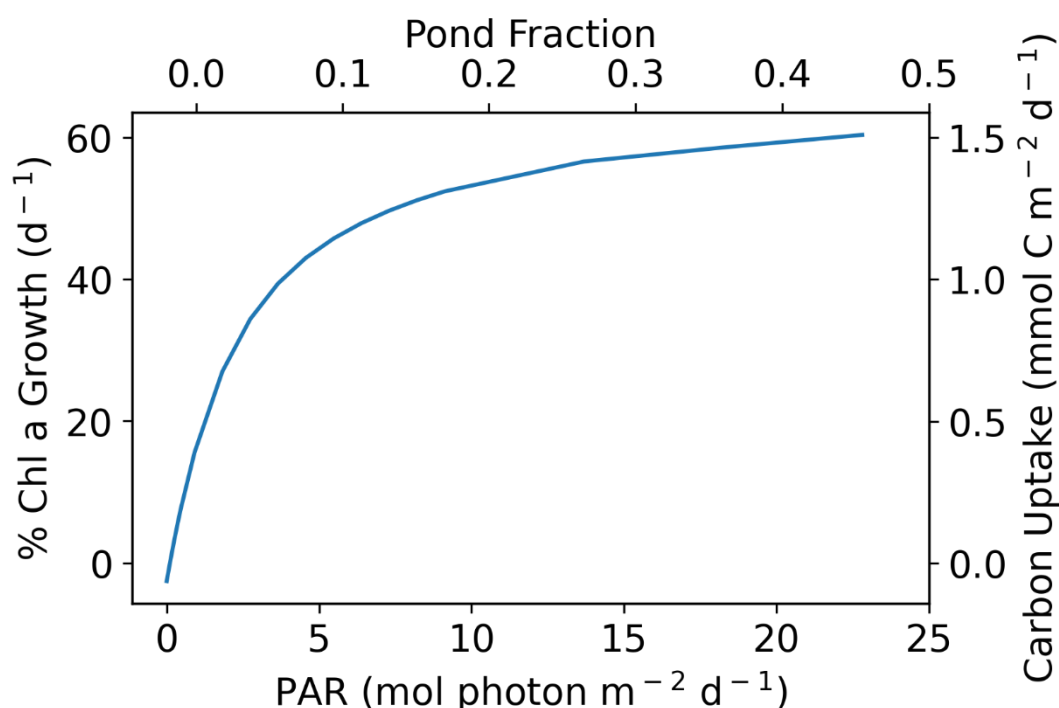
Figure 21: Primary Production Model Results. Production parameters as a function of PAR.

Pond fraction is imposed on the upper x-axis by using its linear relationship with PAR (Figure

20).

Differences between light transmissions calculated from the WV imagery and the coarser

resolution, but publicly available NSIDC Sea Ice Concentration data product showed a high

degree of variability (Figure 22). PAR [$E_d(0^-)$] was calculated for local noon to show the

maximum theoretical irradiance received by the upper water column. At the start of the melt

season when pond fraction was low, $E_d(0^-)$ calculated by NSIDC was lower than values calculated from WV images. Once the widespread onset of melt ponds occurred, there was a higher degree of divergence between WV and NSIDC estimations. Differences ranged from -110 µmol m^{-2} s^{-1} on June 22nd, to +243 µmol m^{-2} s^{-1} on June 26th. In July, NSIDC slightly overestimated irradiance by 50 to 80 µmol m^{-2} s^{-1}.
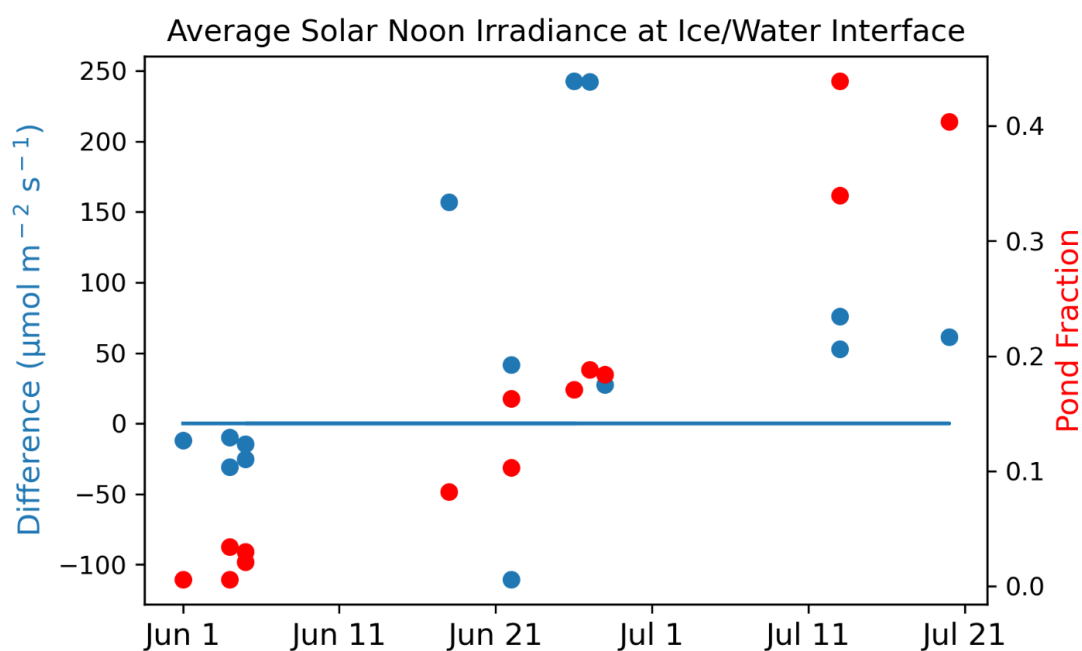
Figure 22: Comparison of WV and NSIDC. Difference in modeled under ice solar noon $E_d(0^-)$ values between NSIDC Sea Ice Concentration and WV images. Difference was calculated by subtracting WV estimates of irradiance from NSIDC estimates, so that a positive difference (above blue line) indicates overestimation by NSIDC, and a negative difference (below blue line) indicates underestimation. Pond fraction is also plotted in red and represented on the right y-axis.

DISCUSSION

Classification Accuracy

The Maximum Likelihood Classifier was able to separate and identify all four classes using RGB imagery, allowing for retrieval of reliable class distribution data. Water and ice classes show the highest degree of accuracy (U-Score) relative to manual classification due to their distinct dark and bright signals, respectively. A low P-Score for ice pixels on scenes from the pond onset phase suggests that certain ice features were misclassified as ponds, since water had a very high U-Score and was not a source of error for the ice pixels.

The MLC performed less well in separating LMP from some ice features during the onset phase. While overall spectra of ice ridges appeared similar to smoother ice, numerous small groupings of blue pixels were present on ridged ice resembling LMPs. This phenomenon was also noticed via ground observations (personal observations of blue tint on ridged sea ice near Barrow, AK). This issue has been found in other attempts to classify ice surfaces as noted by Derksen et al. (1997). However, LMP constitutes such a small portion of the overall scenes during the onset phase (averages <1%) that this misclassification does not greatly impact melt pond coverage estimates. Additionally, it is possible the LMPs were mixed in with ice ridges, as these two features often seem to be co-located (personal observations near Barrow, AK).

Classification accuracy for DMP was also low during onset, due to the presence of shadows cast by snow ridges that were indistinguishable from the DMP spectra. However, snow ridges melted enough by mid-June that this problem disappeared in subsequent images. DMP fraction was also small enough in the onset phase that low accuracy scores did not affect overall analysis of DMP trends. Isolated patches of very thin ice, which appear to be recently refrozen leads, are often classified as DMP. Some misclassifications of ice draft (submerged edges of ice

flows in open water/leads) as DMP also occurred throughout the time series. Ridge shadow and ice draft errors were also reported by Buckley et al. (2020), who concluded that they had small effects on classification accuracy and did not merit any further correction. Additionally, classifying very thin ice and ice draft as melt pond may be advantageous when calculating light transmission or primary production, as these features will propagate more light to the water column than surrounding patches of thicker ice (Tschudi et al., 2001). There were also some misclassifications between DMP and water in the saturation phase, when melt ponds became so dark that their spectral signal began to overlap with that of open water, in agreement with observations from Perovich et al. (2002b). These ponds may have melted all the way through the underlying ice to become open water patches, though this cannot be determined absolutely from satellite imagery alone.

Low U-Scores and high P-Scores for LMP & DMP pixels during the onset phase indicate some over-estimation, though visual inspection showed that melt ponds were not being missed by the MLC. Thus, the classification results appear to represent the maximum possible melt pond fraction. Increased MLC performance in the pond increase and saturation phases is most likely a combination of more true ponds being present for random selection, and the disappearance of snow ridges. These data demonstrate higher confidence during the more dynamic part of the melting cycle.

Though U and P Scores may appear low at times, it is important to remember that they are presenting measurements of over-estimation and under-estimation of a given class by the MLC. As there is no set threshold for deeming U and P Scores as acceptable or unacceptable, these data are somewhat subjective in nature. However, their ability to quantify commonly observed misclassifications and analyze temporal trends in classification accuracy is invaluable.

Throughout all images, there were many small patches of erroneously classified pixels. As there is no non-biased way to exclude these pixels from accuracy validation, they consistently undermine classification accuracy assessments, and often contribute to lowered scores. However, it is important to note the consistent classification accuracy within individual melt ponds across all phases. The common errors discussed here might possibly be resolved by using additional spectral bands with atmospherically corrected signals, so that more data are available to the classifier for teasing apart subtle differences.

Melt Pond Dynamics

Class fraction data reveals a general trend of decreasing ice, which was replaced almost exclusively with an increasing fraction of DMP. Due to the large size (spatial area) of the images, the presence of leads and other open water features did not raise the contribution of the open water class, except for the June 26th data point, which contained the highest recorded water fraction (0.18). The sharp decrease in ice and increase in open water on June 26th was possibly a result of image proximity to the Marginal Ice Zone (MIZ) that marks the transition from open ocean to pack ice, as recorded in the NSIDC Sea Ice Index (Fetterer et al., 2017). Subsequent images were taken further north, away from the MIZ, accounting for the lower open water contribution. It is also possible that a wind event impacted the positioning of ice flows, blowing them further apart on the 26th. This is pure speculation however, as the WARM buoys do not record any wind data.

DMP accounted for the majority of total melt pond area. The difference in color between LMP and DMP is most likely attributed to the underlying ice age and therefore thickness (Tschudi et al., 2001). Consistently low LMP concentrations are explained by the presence of predominantly first-year ice in our images, with few multi-year ice flows identified.

The 3 phases (pond onset, increase, and saturation) presented in this study were specific to this dataset, which contained imagery from 3 segregated temporal periods, each separated by approximately 2 weeks. Though useful for discussing results from these data, these phases are not meant to be broadly applied to other data, or to define specific time periods without careful consideration as to their applicability, as pond development may vary from year to year with geographical location and ice type. Additionally, these phases are not meant to contradict previously established melt pond stages, to include a freeze-up stage not applicable to this study (Eicken et al., 2002; Perovich & Polashenski, 2012).

Another key difference in the data presented here is the lack of an obvious drainage stage, which is often included in other definitions of pond development (Eicken et al., 2002; Fetterer & Untersteiner, 1998; Perovich et al., 2002b; Perovich & Polashenski, 2012). Gaps in imagery leave many days unaccounted for, during which ponds could have drained and re-filled, resulting in no apparent decrease in pond coverage. Alternatively, if individual ice floes drained at different times, the sheer size of a WV scene may have overwhelmed the drainage signal from a handful of ice flows if the majority were not draining. Finally, it is possible that drainage did not occur at all. Fetterer & Untersteiner (1998) noted that smoother first-year ice pond fraction continued to increase, while rougher multi-year ice values decreased from drainage. Additionally, Polashenski et al. (2017) have suggested that melt pond drainage on first-year ice may be inhibited by the freezing of melt water in drainage pathways.

The advantage of having images coincident with in-situ measurements lies in the ability to search for correlations with environmental parameters. Modifying the independent variable to reflect these parameters allows for the exploration of the relationships that drive pond formation. By basing melt pond relationships on an environmental proxy for date, modeling of melt pond

growth can be applied to past or future datasets, provided they contain the necessary measurements. This independence from calendar date is essential when predicting how temporal trends of melt pond development are changing over decadal timescales, and to what extent this process may be altered due to climate change.

As previously mentioned, cumulative hours of above freezing (air temperature) presented the strongest relationship with pond fraction among in-situ data parameters. Despite increasing pond fraction, daily average PAR began to decrease in July, likely due to cloudiness. It is well documented that the Arctic experiences asymmetrical variation in solar insolation around the solstice, with a positive bias towards spring, as irradiance is usually reduced by cloud cover as ice continues to melt (Bernhard et al., 2007).

Unsurprisingly, ponding seems to be driven by prolonged exposure to temperatures above the freezing point of fresh water. Daily average air temperature did not produce a significant relationship with pond fraction, agreeing with previous results (Derksen et al., 1997; Fetterer & Untersteiner, 1998), and stressing the importance of looking at cumulative environmental conditions as predictors, rather than just those conditions present on the day of a measurement. Although pond growth data have displayed highly linear relationships in the past (Derksen et al., 1997), the logistic growth function used here appears to provide a better representation of the mechanics of melt pond development.

Qualitatively, the logistic curve matches observations of few ponds in the onset phase, followed by steep growth during the increase phase, and ending with a plateau during the saturation phase before complete ice disintegration. This progression mirrors the ice-albedo feedback mechanism in which ice albedo remains high in the spring, before a sharp decrease associated with rapid pond formation (Perovich et al., 2002a). When ponds initially form in

groupings on a patch of ice, they effectively lower the local albedo, allowing for increased heat flux into the system, therefore enhancing continued melting.

Quantitatively, the logistic curve showed better predictability for data from all three phases, whereas the linear model overestimated pond fraction before 800 hours above freezing, and underestimated pond fraction past 800 hours above freezing. The discrepancy between the two data points around 1,000 hours above freezing is most likely also due to proximity to the MIZ. The higher pond fraction value corresponds to an image peripherally located to the MIZ, approximately 200km south of the lower pond fraction value recorded on the same day.

Individual Pond Size

Individual ponds seem to be predominantly small (<100 m^2), supporting previous studies (Huang et al. 2016; Luthje et al. 2006; Perovich & Tucker, 1997; Perovich et al. 2002b; Tschudi et al., 2001; Yackel et al., 2000). Median pond surface areas of 3 to 6 m^2 across all three dates are in general agreement with some previously reported values (Huang et al., 2016; Perovich et al., 2002), but lower than others (Perovich & Tucker, 1997; Tschudi et al., 2001), which may possibly be attributed to geographic variability. Huang et al. (2016) noted a similar small median pond size for a site at 72N, with pond sizes increasing as the transect moved northward. Predominating ice type may play a role in controlling pond size, as MYI generally seemed to contain fewer, but larger ponds than FYI. This observation agrees with Nasonova et al. (2018), who observed flooded patches of MYI that had pond fraction values as high as 0.77, despite MYI having lower pond fraction than FYI overall. An attempt to interpret mean pond size was not made, as pond sizes were non-normally distributed.

Pond density values found here were higher than those previously reported (Perovich & Tucker, 1997, Perovich et al., 2002b). Again, this is likely due to predominating ice type, as FYI generally ponds to a greater degree than MYI (Buckley et al., 2020; Fetterer & Untersteiner, 1998; Nasonova et al., 2018; Polashenski et al., 2012). Caution should also be exercised when choosing a minimum acceptable pond size, as this threshold is shown to have a large impact on the resulting data.

Despite dominating the total number of ponds, the smallest ponds (<10 m^2) accounted for a lower fraction of total pond area. Additionally, a clear shift in the distribution of pond sizes normalized to total pond area occurred across the three dates. The transition from small ponds on June 18th, to medium ponds on June 28th, and finally to large ponds on July 20th demonstrates that total pond area increased, despite the appearance of numerous small ponds that decreased median pond size.

The mechanism driving the temporal evolution of pond size was almost certainly the interconnection of ponds formed by the merger of adjacent ponds and the formation of complex channels. Ponds began to grow larger during the increase phase and appeared to dramatically increase during the saturation phase. When ponds melt together and interconnect, they are treated as one continuous patch, explaining low pond density and the presence of increasingly large ponds on July 20th, supporting results presented in Yackel et al. (2000). Pond interconnection has been widely observed in several other studies. Fetterer & Untersteiner (1998) observed ponds interconnecting on young, smooth ice. Perovich & Tucker (1997) note that larger ponds are comprised of smaller ponds connected by tributaries, which was confirmed by a modeling study (Luthje et al., 2006). Tschudi et al. (2001) suggest that interconnection of ponds that have melted through the ice may facilitate the decay of an ice pack. This hypothesis

is supported by our analysis, which shows a heavily interconnected surface on July 20th

preceding images of decayed ice on July 21st.

These observations raise the question- what defines an individual melt pond?

Quantitatively speaking, and in respect to this study, many small and medium sized ponds

connected to each other by even a few pixels are defined as one large pond. However, it is

important to understand that a large pond does not necessarily correspond to a bright, uniform

under ice light environment. Small patches of ice still remained amidst large, interconnected

ponds, and prevented complete surface flooding. These "ice islands" may have been the

remnants of pre-existing snow dunes (sastrugi) formed earlier in the year as described in Petrich

et al (2012) and cause the under-ice light field to become very heterogeneous.

Light Availability

Melt ponds presented a strong relationship with predicted under-ice light values. Their

distribution across large floes contributes to an under-ice light field that may be adequate for

driving primary production in the water column. Leads and other patches of open water have the

potential to allow for high levels of localized production, but on average account for less than

5% of a scene. Thinning ice also increases light availability, which is accounted for in Table 2,

but reaches a cap at 10% transmission.

The relationship between melt pond fraction and potential primary production produces a

saturation-like response reminiscent of a P vs I curve (Kirk, 1994; Platt et al., 1982). As ponding

begins, even a small increase in melt pond fraction, and thus light availability, has a large impact

on potential phytoplankton growth. After this point, increases in irradiance and pond fraction

result in slower increases in growth, eventually reaching a saturating upper limit. These data

suggest that even low levels of ponding could provide enough light to support under-ice production. Therefore, detection of ponds early in their development can make a large difference in the ability to predict under ice blooms. Thus, pond fraction may become an important new predictor variable to drive primary production that reflects the condition of local sea ice. These relationships are widely applicable to Arctic primary production models and have the potential to increase our ability to predict the onset of under-ice phytoplankton blooms based on observations of melt pond distribution.

It is also important to understand the limitations of using a simple model to describe a complex light environment. These light availability estimates describe a light field that accounts for the class distribution of an entire scene. Therefore, the phytoplankton assemblage would be expected to spend proportional amounts of time under each class (Water, LMP, DMP, Ice) throughout the day. In theory this provides robust estimates of average irradiance values available for photosynthesis. However, phytoplankton may experience disproportionate amounts of time in various light environments, depending on the horizontal advection of the ice and water. Additionally, light intensity varies throughout the day, so that a phytoplankton under a given melt pond in the morning may experience a different light environment than under that same pond in the afternoon.

The ability to account for melt ponds when modeling light in the water column made a measurable difference when compared to a single-value sea ice concentration. This is especially true during the pond increase phase. Though high-resolution imagery may not be necessary for predicting primary production in the onset phase when ponds are few, or in the saturation phase when sea ice is covered with dark ponds, the sub-meter spatial resolution shows a clear increase in light availability through the end of June as ponds increase, whereas the light availability

derived from NSIDC Ice Concentration is highly variable. This is due to NSIDC's inability to detect individual melt ponds, instead looking at the average reflectance of a 25 x 25 km pixel. The pond increase phase (late June) is arguably the most important time to model primary production, as blooms have been observed in this period (Ardyna et al., 2020; Hill et al., 2018). Underestimation of light by NSIDC during pond onset is due to its inability to detect small open water leads and sparse pond features, whereas its overestimation during the saturation phase is a result of heavy ponding darkening the 25km pixels, therefore resulting in a low sea ice concentration from the NSIDC algorithm.

Limitations

The task-based nature of WV satellites imposes certain restrictions on revisit time, resulting in irregular temporal resolution. This is clearly manifested in the data presented here, as two large gaps exist from June 6th to June 17th, and June 29th to July 12th. In addition to continuing to exploit high spatial resolution satellite imagery to observe melt ponds, the advantages of higher temporal resolution must also be considered for future studies. As private companies continue to put high resolution imaging platforms into orbit, frequent revisits over a given region are becoming increasingly possible. Over 150 task-based satellites from Planet Labs Inc. have either 0.5 m or 3.7 m spatial resolution, and contain 4 spectral bands (red, green, blue, near-infrared). These systems could be used for similar analysis and offer regular revisits (at least weekly).

The geographic location, spatial scales, and predominant ice type are all important factors that contribute to melt pond dynamics and development, potentially resulting in considerable variability between studies. Therefore, careful consideration should be exercised when

comparing these results to studies conducted outside the Chukchi Sea, at smaller spatial scales, or on primarily MYI or land fast ice. A logistic style growth of pond fraction supports observations presented here but may be inappropriate when applied to other datasets. Further investigation into pan-Arctic pond development on FYI should be conducted before wide implementation of a logistic growth curve is adopted.

As with any emerging field, data are always in short supply. Time series of melt pond fraction spanning the entire melting season are sparse, especially on FYI. The transition from MYI to FYI in tandem with emerging systems capable of observing individual ponds from space demand increased attention and resources be allocated to monitoring inter-annual variability in the seasonal development of melt ponds on FYI.

Future Implications

With the progression of satellites that rival the spatial resolution of airborne cameras, it is more important than ever to take advantage of these platforms for observing changes in earth's most vulnerable ecosystems. Spaceborne imaging systems capable of discerning individual melt ponds are now accessible at a fraction of the cost and labor to the investigator when compared with the effort of establishing an ice camp or making continuous flights over sea ice. The launch of NASA's ICESat-2 platform in 2018 presents promising opportunities to detect and analyze melt pond presence and depth via onboard LiDAR instrumentation, but will continue to require high resolution imagery for validation (Tilling et al., 2020).

Previous melt pond studies have often been constrained to sub-regional scales. The altitude and swath of WV satellite imagery allowed for images spanning hundreds of square kilometers to survey an area encompassing much of the Chukchi Sea. Fetterer & Untersteiner

(1998) suggest that pond coverage variability is minimized when image size exceeds 30 km^2, further necessitating the use of remote sensing instrumentation capable of covering larger areas. It is important to stress the scope of this work as a large-scale regional study, of which more variability should be expected as opposed to repeated observations of the same small group of ice flows.

As the Arctic continues to experience a transition from MYI to FYI, it will be imperative to specifically include parameters to approximate energy balance and photosynthesis under an FYI environment. The models of pond growth, light availability, and primary production presented here represent novel estimates for a system predominantly composed of FYI. Though results in this study will help advance our understanding of melt ponds, the necessity for additional high-resolution images cannot be understated. Moving forward, the ability to create time series of melt pond development on a yearly basis would provide untold insights into the inter-annual variability of the Arctic melt cycle, as well as any long-term decadal scale changes in melt pond development and distribution.

CONCLUSIONS

As the Arctic continues to experience unprecedented changes, it is imperative to examine melt pond behavior on FYI, and how they impact the underlying water column. Melt ponds were successfully classified from high resolution RGB Worldview images mainly comprised of FYI. Images from the Chukchi Sea were largely un-ponded in early June, and experienced pond growth throughout late June and July, reaching melt pond fractions exceeding 0.4. Cumulative hours above freezing (air temperature) was the strongest environmental predictor when modeling melt pond growth with a logistic growth curve ($r^2 = 0.96$). When normalized to total pond area, pond size increased as the melt season continued, a process driven by the interconnection of ponds.

Initial increases in ponding resulted in a steep rise in potential primary production, which begins saturating when pond fraction continued to increase past 0.2. Estimating under-ice light with WorldView images shows a clear increase in $E_d(0^-)$ as ponding increases in late June, a trend which NSIDC passive microwave measurements are unable to detect. These conclusions showcase new insights into FYI melt pond dynamics, distribution patterns, and their resulting effects on under-ice light availability and primary production.

REFERENCES

Ardyna, M., Mundy, C.J., Mayot, N., Matthes, L.C., Oziel, L., …& Arrigo, K. (2020). Under-Ice Phytoplankton Blooms: Shedding Light on the "Invisible" Part of Arctic Primary Production. *Frontiers in Marine Science, 7*. https://doi.org/10.3389/fmars.2020.608032

Arndt, S. & Nicolaus, M. (2014). Seasonal cycle and long-term trend of solar energy flux through Arctic sea ice. *The Cryosphere, 8*, 2219-2233. https://doi.org/10.5194/tc-8-2219-2014

Arrigo, K.R., Perovich, D.K., Pickart, R.S., Brown, Z.W., van Dijken, G.L., Lowry, K.E., …& Swift, J.H. (2014). Phytoplankton blooms beneath the sea ice in the Chukchi sea. *Deep-Sea Research II, 105,* 1-16. https://doi.org/ 10.1016/j.dsr2.2014.03.018

Arrigo, K.R., Mills, M.M., van Dijken, G.L., Lowry, K.E., Pickart, R.S., & Schlitzer, R. (2017). Late Spring Nitrate Distributions Beneath the Ice-Covered Northeastern Chukchi Shelf. *Journal of Geophysical Research: Biogeosciences, 122*, 2409-2417. https://doi.org/ 10.1002/2017JG003881

Assmy, P., Fernández-Méndez, M., Duarte, P., Meyer, A., Randelhoff, A., Mundy, C.J., …& Granskog, M.A. (2017). Leads in Arctic pack ice enable early phytoplankton blooms below snow-covered sea ice. *Scientific Reports, 7*(40850). https://doi.org/ 10.1038/srep40850

Bernhard, G., Booth, C.R., Ehramjian, J.C., Stone, R., & Dutton, E.G. (2007). Ultraviolet and visible radiation at Barrow, Alaska: Climatology and influencing factors on the basis of verion 2 National Science Foundation network data. *Journal of Geophysical Research, 112*. https://doi.org/10.1029/2006JD007865

Buckley, E.M., Farrell, S.L., Duncan, K., Connor, L.N., Kuhn, J.M., & Dominguez, R.T. (2020). Classification of Sea Ice Summer Melt Features in High-Resolution IceBridge Imagery. *Journal of Geophysical Research: Oceans, 125,* e2019JC015738. https://doi.org/ 10.1029/2019JC015738

Chavez Jr., P.S. (1996). Image-Based Atmospheric Corrections- Revisited and Improved. *Photogrammetric Engineering & Remote Sensing, 62*(9), 1025-1036.

Chen, D., & Stow, D. (2002). The Effect of Training Strategies on Supervised Classification at Different Spatial Resolutions. *Photogrammetric Engineering & Remote Sensing, 68*(11), 1155-1161.

Comiso, J.C. (2011). Large Decadal Decline of the Arctic Multiyear Ice Cover. *Journal of Climate, 25*, 1176-1193. https://doi.org/ 10.1175/JCLI-D-11-00113.1

Derksen, C., Piwowar, J., & LeDrew, E. (1997). Sea-Ice Melt-Pond Fraction as Determined from Low Level Aerial Photographs. *Arctic and Alpine Research, 29*(3), 345-351. https://doi.org/ 10.1080/00040851.1997.12003254

DigitalGlobe. (2009). WorldView-2 Overview. www.digitalglobe.com

DigitalGlobe. (2013). WorldView-3 Data Sheet. www.digitalglobe.com

Eicken, H., Krouse, H.R., Kadko, D., & Perovich, D.K. (2002). Tracer studies of pathways and rates of meltwater transport through Arctic summer sea ice. *Journal of Geophysical Research, 107*(C10), 8046. https://doi.org/ 1029/2000JC000583

Fetterer, F., & Untersteiner, N. (1998). Observations of melt ponds on Arctic sea ice. *Journal of Geophysical Research, 103*(C11), 24821-24835. https://doi.org/10.1029/98JC02034

Fetterer, F., K. Knowles, W. N. Meier, M. Savoie, and A. K. Windnagel. (2017, updated daily). *Sea Ice Index, Version 3*. [June 26th, 2018]. Boulder, Colorado USA. NSIDC: National Snow and Ice Data Center.

Forest, A., Tremblay, J.E., Gratton, Y., Martin, J., Gagnon, J., Darnis, G., …& Piepenburg, D. (2011). Biogenic carbon flows through the planktonic food web of the Amundsen Gulf (Arctic Ocean): A synthesis of field measurements and inverse modeling analyses. *Progress in Oceanography, 91*(4), 410-436. https://doi.org/10.1016/j.pocean.2011.05.002

Frey, K.E., Perovich, D.K., & Light, B. (2011). The spatial distribution of solar radiation under a melting Arctic sea ice cover. *Geophysical Research Letters, 38*(L22501). https://doi.org/doi:10.1029/2011GL049421

Grebmeier, J.M. (2012). Shifting Patterns of Life in the Pacific Arctic and Sub-Arctic Seas. *Annu. Rev. Mar. Sci., 4*, 63-78. https://doi.org/10.1146/annurev-marine-120710-100926

Hill, V. (2004). The Western Arctic Shelf-Basin Interactions (SBI) experiment contains measurements made in the Chukchi and Beaufort seas off the coast of northern Alaska. *NASA SeaBASS*.

Hill, V.J., Light, B., Steele, M., & Zimmerman, R.C. (2018). Light Availability and Phytoplankton Growth Beneath Arctic Sea Ice: Integrating Observations and Modeling. *Journal of Geophysical Research: Oceans, 123,* 3651-3667. https://doi.org/10.1029/2017JC013617

Hill, V. (2019). Warming and irradiance Measurement (WARM) buoys deployed in Canada Basin and Chukchi Shelf, Arctic Ocean, 2018. *Arctic Data Center*. https://doi.org/10.18739/A2NP1WJ27

Huang, W., Lu, P., Lei, R., Xie, H., & Li, Z. (2016). Melt pond distribution and geometry in high Arctic sea ice derived from aerial investigations. *Annals of Glaciology, 57*(73), 105-118. https://doi.org/10.1017/aog.2016.30

Ji, R., Jin, M., & Varpe, Ø. (2013). Sea ice phenology and timing of primary production pulses in the Arctic Ocean. *Global Change Biology, 19*, 734-741. https://doi.org/10.1111/gcb.12074

Johnson, M., & Eicken, H. (2016). Estimating Arctic sea-ice freeze-up and break-up from the satellite record: A comparison of different approaches in the Chukchi and Beaufort Seas. *Elementa: Science of the Anthropocene, 4*(000124). https://doi.org/10.12952/journal.elementa.000124

Kieber, D.J., McDaniel, J., & Mopper, K. (1989). Photochemical source of biological substrates in sea water: implications for carbon cycling. *Nature, 341*, 637-639. https://doi.org/10.1038/341637a0

Kirk, J.T.O. (1994). Light & Photosynthesis in Aquatic Ecosystems, Second Edition. *Cambridge University Press, New York, NY*.

Light, B., Grenfell, T.C., & Perovich, D.K. (2008). Transmission and absorption of solar radiation by Arctic sea ice during the melt season. *Journal of Geophysical Research, 113*(C03023). https://doi.org/10.1029/2006JC003977

Light, B., Perovich, D.K., Webster, M.A., Polashenski, C., & Dadic, R. (2015). Optical properties of melting first-year Arctic sea ice. *Journal of Geophysical Research: Oceans, 120*. https://doi.org/10.1002/2015JC011163

Lüthje, M., Feltham, D.L., Taylor, P.D., & Worster, M.G. (2006). Modeling the summertime evolution of sea-ice melt ponds. *Journal of Geophysical Research, 111*(C02001). https://doi.org/10.1029/2004JC002818

McGarigal, K., Cushman, SA., & Ene, E. (2012). FRAGSTATS v4: Spatial Pattern Analysis Program for Categorical and Continuous Maps. Computer software program produced by the authors at the University of Massachusetts, Amherst. Available at the following web site: http://www.umass.edu/landeco/research/fragstats/fragstats.html

Mobley, C.D., Cota, G.F., Grenfell, T.C., Maffione, R.A., Pegau, W.S., & Perovich, D.K. (1998). Modeling Light Propagation in Sea Ice. *IEEE Transactions on Geoscience and Remote Sensing, 36*(5). https://doi.org/10.1109/36.718642

Nasonova, S., Scharien, R.K., Haas, C., & Howell, S.E.L. (2018). Linking Regional Winter Sea Ice Thickness and Surface Roughness to Spring Melt Pond Fraction on Landfast Arctic Sea Ice. *Remote Sensing, 10*(37). https://doi.org/10.3390/rs10010037

Nicolaus, M., Katlein, C., Maslanik, J., & Hendricks, S. (2012). Changes in Arctic sea ice result in increasing light transmittance and absorption. *Geophysical Research Letters, 39*(L24501). https://doi.org/10.1029/2012GL053738

Olofsson, P., Foody, G.M., Stehman, S.V., & Woodcock, C.E. (2013). Making better use of accuracy data in land change studies: Estimating accuracy and area and quantifying uncertainty using stratified estimation. *Remote Sensing of Environment*, *129*, 122-131. http://dx.doi.org/10.1016/j.rse.2012.10.031

Perovich, D.K. & Maykut, G.A. (1990). Solar Heating of a Stratified Ocean in the Presence of a Static Ice Cover. *Journal of Geophysical Research, 95*, 18,233-18,245. https://doi.org/10.1029/JC095iC10p18233

Perovich, D.K., & Tucker III, W.B. (1997). Arctic sea-ice conditions and the distribution of solar radiation during summer. *Annals of Glaciology, 25,* 445-450. https://doi.org/10.3189/S0260305500014439

Perovich, D.K., Roesler, C.S., & Pegau, W.S. (1998a). Variability in Arctic sea ice optical properties. *Journal of Geophysical Research, 103*(C1), 1193-1208. https://doi.org/10.1029/97JC01614

Perovich, D.K., Longacre, J., Barber, D.G., Maffione, R.A., Cota, G.F., Mobley, C.D., …& Roesler, C.S. (1998b). Field Observations of the Electromagnetic Properties of First-Year Sea Ice. *IEEE Transactions on Geoscience and Remote Sensing, 36*(5), 1705-1715. https://doi.org/10.1109/36.718639

Perovich, D.K., Grenfell, T.C., Light, B., & Hobbs, P.V. (2002a). Seasonal evolution of the albedo of multiyear Arctic sea ice. *Journal of Geophysical Research, 107*(C10), 8044. https://doi.org/10.1029/2000JC000449

Perovich, D.K., Tucker III, W.B., & Ligett, K.A. (2002b). Aerial observations of the evolution of ice surface conditions during summer. *Journal of Geophysical Research, 107*(C10), 8048. https://doi.org/10.1029/2000JC000438

Perovich, D.K. (2007). Light reflection and transmission by a temperate snow cover. *Journal of Glaciology, 53*(181), 201-210. https://doi.org/10.3189/172756507782202919

Perovich, D.K., Richter-Menge, J.A., Jones, K.F., & Light, B. (2008). Sunlight, water, and ice: Extreme Arctic sea ice melt during the summer of 2007. *Geophysical Research Letters. 35*(L11501). https://doi.org/10.1029/2008GL034007

Perovich, D.K., & Polashenski, C. (2012). Albedo evolution of seasonal Arctic sea ice. *Geophysical Research Letters, 39*(L08501). https://doi.org/doi:10.1029/2012GL051432

Perumal, K., & Bhaskaran, R. (2010). Supervised Classification Performance of Multispectral Images. *Journal of Computing, 2(2),* 124-129.

Petrich, C., Eicken, H, Polashenski, C.M., Sturm, M., Harbeck, J.P., Perovich, D.K., & Finnegan, D.C. (2012). Snow dunes: A controlling factor of melt pond distribution on Arctic sea ice. *Journal of Geophysical Research, 117*(C09029). https://doi.org/10.1029/2012JC008192

Pinkerton, M.H. & Hayward, A. (2021). Estimating variability and long-term change in sea ice primary productivity using a satellite-based light penetration index. *Journal of Marine Systems, 221*. https://doi.org/10.1016/j.jmarsys.2021.103576

Platt, T., Harrison, W.G., Irwin, B., Horne, E.P., & Gallegos, C.L. (1982). Photosynthesis and photoadaptation of marine phytoplankton in the Arctic. *Deep-Sea Research, 29*(10A), 1159-1170. https://doi.org/10.1016/0198-0149(82)90087-5

Polashenski, C., Perovich, D., & Courville, Z. (2012). The mechanisms of sea ice melt pond formation and evolution. *Journal of Geophysical Research, 117*(C01001). https://doi.org/10.1029/2011JC007231

Polashenski, C., Golden, K.M., Perovich, D.K., Skyllingstad, E., Arnsten, A., Stwertka, C., & Wright, N. (2017). Percolation blockage: A process that enables melt pond formation on first year Arctic sea ice. *Journal of Geophysical Research: Oceans, 122,* 413-440. https://doi.org/10.1002/2016JC011994

Richter-Menge, J., & Druckenmiller, M.L. (2020). State of the Climate in 2019: The Arctic. *Bulletin of the American Meteorological Society, 101*(8), S239-S286. https://doi.org/10.1175/BAMS-D-20-0086.1

Sulzberger, B., & Arey, J.S. (2016). Impacts of Polar Changes on the UV-induced Mineralization of Terrigenous Dissolved Organic Matter. *Environmental Science and Technology, 50*, 6621-6631. https://doi.org/10.1021/acs.est.5b05994

Tilling, R., Kurtz, N.T., Bagnardi, M., Petty, A.A., & Kwok, R. (2020). Detection of Melt Ponds on Arctic Summer Sea Ice From ICESat-2. *Geophysical Research Letters, 47,* e2020GL090644. https://doi.org/10.1029/2020GL090644

Tschudi, M.A., Curry, J.A., & Maslanik, J.A. (2001). Airborne observations of summertime surface features and their effect on surface albedo during FIRE/SHEBA. *Journal of Geophysical Research, 106*(D14), 15335-15344. https://doi.org/10.1029/2000JD900275

Tschudi, M.A., Maslanik, J.A., & Perovich, D.K. (2008). Derivation of melt pond coverage on Arctic sea ice using MODIS observations. *Remote Sensing of Environment, 112,* 2605-2614. https://doi.org/10.1016/j.rse.2007.12.009

Webster, M.A., Rigor, I.G., Perovich, D.K., Richter-Menge, J.A., Polashenski, C.M., & Light, B. (2015). Seasonal evolution of melt ponds on Arctic sea ice. *Journal of Geophysical Research: Oceans, 120,* 5968-5982. https://doi.org/10.1002/2015JC011030

Yackel, J.J., Barber, D.G., & Hanesiak, J.M. (2000). Melt ponds on sea ice in the Canadian Archipelago 1. Variability in morphological and radiative properties. *Journal of Geophysical Research, 105*(C9), 22049-22060. https://doi.org/10.1029/2000JC900076

VITA

Austin Wesley Abbott
Department of Ocean and Earth Sciences
Old Dominion University
4600 Elkhorn Ave.
Norfolk, VA 23529

Education

August 2021 M.S., Ocean and Earth Sciences
Dept. of Ocean and Earth Sciences (OES), Old Dominion University

August 2017 B.S., Biology
College of Biological Sciences, University of Minnesota Twin-Cities

Conference Presentations

ODU GRAD Day Poster Competition, April 5-9, 2021
"Using High Resolution Satellite Imagery to Examine Melt Ponds on Arctic Sea Ice"

Alaska Marine Science Symposium, January 26-28, 2021
"Examining Arctic Melt Pond Dynamics via High Resolution Satellite Imagery"

Ocean Sciences 2020, February 16-21, 2020, San Diego, CA
"Using High Resolution Satellite Imagery to Examine Melt Pond Variability in the Arctic"

Earth System Modeling Graduate Symposium, April 11, 2019, George Mason University
"Using High Resolution Satellite Imagery to Quantify Ice Cover and Light Transmission to the Upper Water Column"

Leadership and Awards

Graduate Student Summer Award Program   Summer 2021

Dorothy Brown Smith Travel Award   Spring 2020

Vice-President, OES Graduate Student Organization   Fall 2019 – Spring 2020